Numerical Simulations of Pool-Boiling Heat Transfer

Vijay K. Dhir
Mechanical and Aerospace Engineering Dept., University of California, Los Angeles, Los Angeles, CA 90095

Boiling has been studied extensively during the last half of the 20th century. Many correlations and semimechanistic models have also been developed for various modes of boiling. However, due to the complexity involved in modeling continuously evolving vapor–liquid interfaces, unrealistic assumptions are often made in developing various models. With the advances of recent years in the area of computational science and engineering, it is now possible to solve, completely, the conservation equations of mass, momentum, and energy for liquid and vapor phases simultaneously when an interface is continuously evolving at and near a heated surface. The solutions provide not only detailed physics of associated thermal and hydrodynamic processes, but also the shape of the evolving interface. In demonstrating the application of numerical simulations as an effective tool, both pool nucleate and film boiling at normal earth gravity, and nucleate boiling under microgravity conditions are considered. Although these simulations have been computationally intensive, in the future calculations of this type are expected to become routine.

Introduction

During the last half of the twentieth century boiling under pool and forced flow conditions has been studied extensively. The impetus for these studies comes not only from the fact that boiling allows accommodation of very high heat fluxes at relatively low wall superheats but also because the process is very complex and its understanding imposes significant challenges.

The past efforts can be grouped into two broad categories. In the first category are the studies in which data for boiling heat transfer has been obtained as a function of any of the several independent variables such as heater size, shape, and surface condition, heater thickness, heating method, liquid temperature, system pressure, liquid and vapor thermophysical properties, heater confinement, and flow conditions. The data have been correlated with semimechanistic models or dimensionless groups involving independent and dependent variables. The correlations have been helpful in application of the results to practical situations. However, the correlations serve their useful purpose only when they are applied in the range of the database used in developing the correlations.

The studies in the second category are those that have focused on detailed investigation of individual subprocesses with the hope that such studies will serve as a basis for the development of mechanistic models for the prediction of boiling heat fluxes as a function of wall superheat or other independent variables. The list includes, but is not limited to, studies on inception superheat, nucleation-site density, bubble dynamics, fractional area of liquid–solid contacts and their duration, mechanisms of heat transfer, interfacial instabilities, and interfacial heat and mass transfer. Sadly, however, these basic studies of individual phenomena have been rarely successful in meeting their final objective. This is due to the fact that as the studies have not been able to properly include the interactions that take place among various subprocesses. For example, bubble dynamics can strongly influence the heat transfer associated with microlayer, evaporation around the vapor bubble interface, and convection motion created by the bubble during its growth and departure and vice versa.

Nucleate boiling

Phenomenologically, boiling can be broadly divided into three modes: nucleate, transition, and film boiling. Nucleate boiling at low wall superheats (partial) is characterized by the release of discrete bubbles from randomly located active sites. The frequency of bubble release and number density of active nucleation sites increase with wall superheat. The transi-

tion from partial to fully developed nucleate boiling occurs when bubbles at a given site begin to merge in the vertical direction. Now vapor appears to leave the heater in the form of jets. The condition of jet formation approximately coincides with merger of vapor bubbles at neighboring sites. After lateral merger, vapor structures appear that look like mushrooms with several stems.

Without distinguishing the phenomenological differences that exist between partial and fully developed nucleate boiling, Rohsenow (1952) proposed a correlation (first category) that was applicable to both the discrete and mushroom type of bubble regime. Although the correlation was not based on conceptually correct physics as recognized later by the author himself (1969), the correlation has been widely used. Subsequently, Stephen and Abdelsalam (1980) developed a comprehensive correlation for saturated nucleate pool boiling of different liquids. The correlation employs dimensionless groups based on both fluid and solid properties, but no consideration is given to heater geometry. Cooper (1984a,b) has proposed a simple correlation for saturated nucleate pool boiling. The correlation uses reduced pressure, molecular weight, and surface roughness as the correlating parameters. Although the correlation accounts for heater surface roughness, it does not include the effect of surface wettability. Also, the lead constant in the correlation is found to depend on the geometry of the heater. As should be evident from the preceding description, these correlations are not universal and large deviations between actual data and predictions can occur when conditions for which the correlations were developed are not duplicated.

To mechanistically model nucleate boiling, past efforts (second category) have been devoted to inception, nucleation site density, bubble dynamics, which includes bubble growth and departure, and the associated heat-transfer processes. The superheat required for cavities to nucleate on a surface is much smaller than that required for homogeneous nucleation. This is due to the fact that vapor/gas trapped in the imperfections on the heated surface serves as nuclei for bubbles.

Bankoff (1958) was the first to suggest that a wedge-shaped imperfection on a surface will trap vapor/gas as long as contact angle of the advancing liquid front is greater than the wedge angle. Subsequently Wang and Dhir (1993a), among others, have developed an alternate criterion for entrapment of vapor/gas in cavities. According to their criterion, a cavity will trap vapor/gas only if the contact angle is greater than the cavity mouth angle.

Hsu (1962) was the first to propose a criterion for the superheat required for a cavity to nucleate. According to Hsu's criterion, an embryo will evolve into a bubble if the temperature of the liquid at the tip of the embryo is at least equal to saturation temperature corresponding to pressure in the bubble. In the alternate approach, which has been commonly used, it is proposed that boiling incipience corresponds to a critical point of instability of the vapor–liquid interface. The interface is considered to be stable or quasi stable if the curvature of the interface increases with increase in vapor volume.

Utilizing the instability concept and noting that nucleation occurs when the nondimensional curvature of the interface outside of the cavity attains a maximum value, Wang and Dhir (1993a) obtained a relation between superheat and cavity diameter as

$$\Delta T = \frac{4\sigma T_{\text{sat}}}{\rho_v h_{fg} D_c} K_{\max}, \tag{1}$$

where $K_{\max}$ is the dimensionless maximum curvature and has a value of unity for contact angles (φ) less than 90°, but is equal to $\sin\varphi$ for contact angles (φ) greater than 90°. Through carefully conducted experiments Wang (1992) validated Eq. 1.

The number of active nucleation sites increases with wall superheat or wall heat flux. Because the introduction of new nucleation sites influences the rate of heat transfer from the surface, a knowledge of nucleations site density is needed. Several correlations for the nucleation site density as a function of wall superheat or heat flux have been reported in the literature. In general the active site density is correlated as

$$Na \sim \Delta T^{m_1}. \tag{2}$$

The proportionality constant in Eq. 2 depends on the surface wettability and surface roughness. The exponent, m_1, generally varies between 4 and 6, and there is some evidence that it can be affected by the manner in which a surface is prepared.

Wang and Dhir (1993a,b) have provided a mechanistic approach to the determination of the number density of active nucleation sites. Their approach requires a knowledge of size, shape, and mouth angle of all the cavities present in the solid. Additionally, by invoking the gas entrapment and inception superheat criteria, they were able to determine the nucleating fraction of all the cavities present on the heater surface. Another important conclusion from their work is that surface wettability is an important variable and they noted as much as a twentyfold reduction in active cavity site density when the content angle was reduced from 90° and 18° on the same surface. As has been pointed out by Kenning (1989) and Judd and Chopra (1993), thermal and flow conditions in the vicinity of a heated surface can lead to activation of inactive sites and deactivation of active sites. This aspect was not considered in the work of Wang and Dhir.

Bubble dynamics includes the processes of bubble growth, bubble departure, and the waiting period that, when combined with the growth period, yields bubble-release frequency. Bubble growth occurs as a result of evaporation around the bubble surface as well as at the bubble base. Following the earlier work of Plesset and Zwick (1954), Mikic et al. (1970) obtained an analytical solution for the bubble growth rate by using a geometric shape factor to relate the shape of a bubble growing on a heater surface to a perfect sphere, and accounting for the thermal energy stored in the superheated liquid layer prior to inception, but ignoring the contribution of the microlayer. Since the initial energy content of the superheated liquid layer depends on the waiting time, the model shows dependence of growth rate on waiting time.

After Snyder and Edwards (1956) proposed the presence of microlayer evaporation at the bubble base, Cooper and Lloyd (1969) not only confirmed the existence of the microlayer underneath isolated bubbles formed on glass or ceramic

surfaces but also deduced the thickness of the microlayer from the observed response of the heater-surface thermocouple. They noted that an expression for the average thickness, δ, of the microlayer could be written as

$$\delta \sim \sqrt{\alpha_\ell t_g} \tag{3}$$

They further demonstrated that bubble growth was mostly due to evaporation from the microlayer.

The diameter to which a bubble grows before departure is dictated by the balance of forces that act on the bubble. These forces are associated with the inertia of liquid and vapor, the liquid drag on the bubble, buoyancy, and surface tension. Several empirical expressions for bubble departure diameter have been given in the literature, depending on the importance that is given to various forces that act on the bubble. Cole and Rosenow (1969) correlated bubble diameter at departure with fluid properties, but found it to be independent of wall superheat. However, Gorenflow et al. (1986) proposed an expression for the bubble diameter at departure that indicates that the bubble diameter increases weakly with wall superheat. Although it is generally accepted that surface tension tends to hold the bubble to the surface, Cooper et al. (1978) and more recently Buyewich and Webber (1996) have argued that surface tension assists bubble departure by making the bubbles spherical.

The waiting time, t_w, corresponds to the time it takes for the thermal layer to redevelop after the departure of a bubble and allow nucleation of a new bubble. Knowing the bubble diameter at departure and the bubble growth rate, the growth period, t_g, can be calculated, and thus the bubble release frequency. However, because of the uncertainties that exist in the bubble diameter at departure and the waiting time, most often correlations involving bubble diameter at departure and bubble release frequency are given. One such correlation is that due to Melenkov (1971).

Several attempts have been made in the past to use the models for the subprocesses described earlier to develop a global model for partial nucleate boiling. Mikic and Rohsenow (1969), assumed that transient conduction into the liquid during the waiting period over the region influenced by the vapor bubbles and natural convection over the remaining regions of the heater contributed to the total heat transfer. Subsequently, Judd and Hwang (1976) suggested that microlayer contribution should also be included. As such an expression for partial nucleate boiling heat flux was written by superimposing the contributions of the three mechanisms as

$$q = \frac{K^2}{2}\sqrt{\pi\left(k\rho c_p\right)_\ell f}\, D_d^2 Na\Delta T + \left(1 - \frac{K^2}{4} Na\pi D_d^2\right)\bar{h}_{nc}\Delta T + \bar{h}_{ev}\Delta T Na\frac{\pi}{4}D_d^2, \tag{4}$$

where K is the proportionality constant for bubble diameter of influence. Also in writing Eq. 4 it is assumed that transient conduction of heat into the liquid continues during the waiting as well as during the growth periods. Although the consistency of Eq. 4 has been shown by Judd and Hwang (1976) from experiments in which dichloromethane was boiled on a glass surface, the key deficiencies of Eq. 4 are that it does not include the feedback that exists between various mechanisms and it involves several empirical constants that need to be adjusted to match the predictions with the data. Thus, at present we do not have a mechanistic model for partial nucleate boiling that has models that are consistent both at the subprocess level as well as at the global process level.

In fully developed nucleate boiling, when mushroom type of bubbles with several stems attached to the heater surface and vapor columns are present on the surface, evaporation at the base and periphery of these stems is the main mode of heat transfer. Gaertner (1965) provided photographic evidence of these stems. He also provided very valuable data on the size of the vapor stems, their spacing, and wall void fraction as a function of wall superheat. However, he did not use the information to develop a model for fully developed nucleate boiling. Recently, Lay and Dhir (1995) developed a mechanistic model for the prediction of size and shape of the vapor stems as a function of wall superheat and the magnitude of Hamakar constant. In the model it was assumed that the duration for which vapor stems exist on the heater surface is much larger than the time needed to form the stems. Thus, they neglected the transients associated with formation and extinction of vapor stems. By utilizing the approach proposed by Wang and Dhir (1993a) for determination of active nucleation site density, Lay and Dhir (1994) were able to predict the fully developed nucleate boiling heat fluxes as a function of wall superheat. The key weakness of their work is that they did not provide photographic evidence of the shape of the vapor stems and their size, although a corroboration of the predicted stem size with the previously reported data of Gaertner was given.

Film boiling

Studies reported in the literature in the area of film boiling can also be grouped into two categories as defined earlier. Very often for film boiling, however, a sharp distinction between studies of global and subprocess level does not exist, as was the case for nucleate boiling. For example, Berenson (1961) developed a semimechanistic model for saturated film boiling on a horizontal surface. In his area and time-averaged static model, empirical information about vapor bubble spacing, bubble height, and bubble diameter was used. Although, over the years Berenson's model has been found to be very successful in predicting film-boiling heat transfer on horizontal plates, the static model is based on several questionable assumptions. For instance, a film of constant thickness is assumed to connect two neighboring bubbles. Since the vapor flow to each bubble through the film is as a result of hydrostatic head difference, existence of a film of constant thickness is not physically possible.

Similar semimechanistic models for other geometries (such as vertical plates, cylinders, and so on) have been developed by Bromley (1950) and Breen and Westwater (1962). In these models to account for the formation of waves at the interface as the vapor flow path length increases and for the fractional area of the heater occupied by vapor bubbles, empirical constants must be employed.

More recently Sakurai et al. (1990a,b) have developed comprehensive correlations for saturated and subcooled film

boiling on horizontal cylinders. In developing the correlations, which include the effect of radiation, the functional form of the correlations was obtained by solving the conservation equations for a two-layered configuration of subcooled film boiling with a plane interface between the layers. The correlations were validated with a database that covered a wide range of heater diameters, wall superheats, liquid subcoolings, and system pressures. Subsequently Sakurai and Shiotsu (1992) extended those correlations to include a vertical surface and a sphere. Although empirical constants have been adjusted to match the predictions with the data, the physical picture of the process used in the model may not be entirely correct. It is well known that instabilities at the vapor–liquid interface develop at a short distance from the leading edge of a vertical plate. Presence of both short and long waves on the surface significantly alters the flow and thermal field in the vapor and the liquid. Vijaykumar and Dhir (1992a,b) have shown from detailed experiments that during subcooled film boiling on a vertical surface vapor is mostly produced in the thin-film region and is condensed at the interface protruding into liquid. This behavior not only shortens the vapor flow path length but also improves the rate of heat transfer from the wall. Thus, any global model should appropriately account for the interface shape and the heat and mass transfer that takes place at the interface.

We see from the preceding discussion on nucleate and film boiling that in order to have global mechanistic models for boiling heat transfer, it is necessary to have submodels that represent the physics of the process correctly. This physics, however, can only be realized if the thermal and hydrodynamic processes associated with evolving liquid–vapor interfaces are modeled simultaneously, which has not been done in the past. Because of the complexity of the processes involved, it is believed that complete numerical simulations of the process may be the only viable option. Thus, the objective of this article is to demonstrate how numerical simulations can be used to model nucleate and film boiling. This in no way diminishes the importance of the detailed experiments that are essential to validate the results of the numerical simulations both at the subprocess level as well as at the global level.

Numerical Simulations

Although the conservation equation for both vapor and liquid phases in nucleate and film boiling are the same, the physics of the two processes is quite different. As such in the following we describe each process separately.

Nucleate boiling

In partial nucleate boiling the nucleation sites are sparsely populated, and as a result bubble–bubble interactions are not important, and one can focus only on the thermal and hydrodynamic processes at and around a single nucleation site. Because of the symmetry that is expected to exist around the cavity, axisymmantic analysis can be carried out for single bubbles in partial nucleate boiling. However, in fully developed nucleate boiling when bubbles start to merge in the lateral direction, one needs to carry out three-dimensional analysis. In analyzing the growth of a single bubble, Son et al. (1999) divided the computational domain into micro- and macro-regions, as shown in Figure 1. The microregion contains the thin film that forms underneath the bubble, whereas the macroregion consists of the bubble and the liquid surrounding the bubble. In carrying out the analysis, the flow is assumed to be laminar and the fluid properties, including density, viscosity, and thermal conductivity, are evaluated at a mean temperature in each phase. For the microlayer lubrication theory is employed, and it has been used and validated by a number of investigators in the literature (such as Wayner, 1992; Lay and Dhir, 1995).

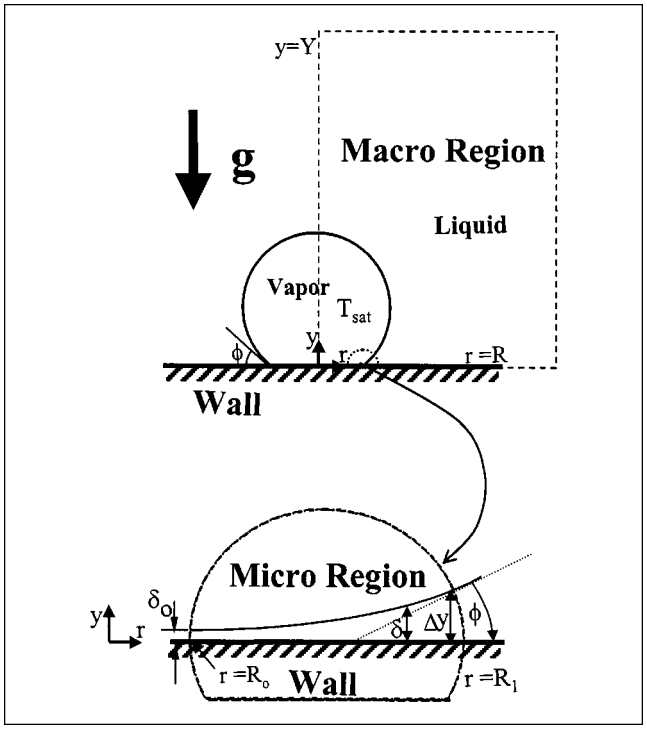

Figure 1. Macro- and microregions used in numerical simulation.

Microregion. The equation of mass conservation in the microlayer is written as

$$\frac{\partial \delta}{\partial t} = v_\ell - q/\rho_\ell h_{fg}. \tag{5}$$

In Eq. 5, the liquid velocity normal to the vapor–liquid interface, v_ℓ, is obtained from the continuity equation as

$$v_\ell = -\frac{1}{r}\frac{\partial}{\partial r}\int_0^\delta r u_\ell \, dy. \tag{6}$$

The momentum equation for the microlayer is written as

$$\frac{\partial p_\ell}{\partial r} = \mu_l \frac{\partial^2 u_\ell}{\partial y^2}. \tag{7}$$

The energy conservation equation for the film yields

$$q = k_\ell (T_W - T_{\text{int}})/\delta. \tag{8}$$

The inertia terms in the momentum equation and convection terms in the energy equation can be neglected because the Reynolds number based on the liquid-film thickness and the liquid velocity (smaller than 0.05 m/s for $\Delta T = 8.5$ K) in the microregion is less than unity.

Using a modified Clausius–Clayperon equation, (such as Wayner, 1992), the evaporative heat flux is written as

$$q = h_{ev}\left[T_{\text{int}} - T_v + (p_\ell - p_v)T_v/\rho_\ell h_{fg}\right], \tag{9}$$

where

$$h_{ev} = 2\left(M/2\pi\bar{R}T_v\right)^{0.5}\rho_v h_{fg}^2/T_v; \qquad T_v = T_{\text{sat}}(p_v). \tag{10}$$

The pressures in the vapor and liquid phases are related (Lay and Dhir, 1995), as

$$p_\ell = p_v - \gamma\kappa - \frac{A}{\delta^3} + \frac{q^2}{\rho_v h_{fg}^2}, \tag{11}$$

where surface tension, γ, is taken to be a function of temperature, and A is the dispersion constant relating disjoining pressure to the film thickness. In Eq. 11, the second term on the righthand side accounts for the capillary pressure, the third term for the disjoining pressure, and the last term originates from the recoil pressure. The curvature of the interface is defined as

$$\kappa = \frac{1}{r}\frac{\partial}{\partial r}\left(r\frac{\partial\delta}{\partial r}\Big/\sqrt{1+\left(\frac{\partial\delta}{\partial r}\right)^2}\right). \tag{12}$$

The combination of the mass, momentum, and energy equations for the microlayer yields

$$\delta'''' = f(\delta, \delta'\delta''\delta'''), \tag{13}$$

where superscript $'$ denotes $\partial/\partial r$.

The boundary conditions for the preceding equation are as follows: at

$$r = R_0, \qquad \delta = \delta_0; \qquad \delta' = \delta''' = 0, \tag{14}$$

where δ_0 is of the order of molecular length (refer to Lay and Dhir, 1995), and at

$$r = R_1, \qquad \delta = h/2; \qquad \delta'' = 0, \tag{15}$$

where $h/2$ is the distance to the first computational node for the level set function, ϕ, from the wall. In implementing the boundary conditions just given, the radius R_1 was determined from the solution of the macroregion. For a given dispersion constant, the microlayer formulation, Eq. 13, and R_0 are solved with five boundary conditions, Eqs. 14 and 15. In this study an apparent contact angle is defined as

$$\tan\varphi = h/2(R_1 - R_0). \tag{16}$$

Macroregion. For numerically analyzing the macroregion, the level-set formulation is used. Other methods, such as volume of fluid (VOF), lattice Boltzman, and direct front tracking, have been used in the literature for capturing the interface and the thermal and hydrodynamic process associated with an evolving interface. For example, Juric and Tryggvason (1995) used the front-tracking method to carry out two-dimensional simulations of the rise and growth of vapor bubbles in a superheated liquid and to simulate the evolution of the vapor–liquid interface during saturated film boiling. In a subsequent paper (1996), they used the same method to investigate directional solidification of a dilute binary alloy and rapid evaporation of a superheated liquid under zero-gravity conditions. In the level-set method, the interface separating the two phases is captured by function ϕ, which is defined as a signed distance from the interface. The negative sign is chosen for the vapor phase and the positive sign for the liquid phase. The momentum and energy equations for the vapor and liquid regions are written as

$$\rho\left(\frac{\partial u}{\partial t} + u\cdot\nabla u\right) = -\nabla p + \rho g - \rho\beta_T(T - T_{\text{sat}})g - \gamma\kappa\nabla H + \nabla\cdot\mu\nabla u + \nabla\cdot\mu\nabla u^T \tag{17}$$

$$\rho c_{pl}\left(\frac{\partial T}{\partial t} + u\cdot\nabla T\right) = \nabla\cdot k\nabla T \qquad \text{for } H > 0$$

$$T = T_{\text{sat}}(p_v) \qquad \text{for } H = 0, \tag{18}$$

where

$$\rho = \rho_v + (\rho_l - \rho_v)H$$

$$\mu^{-1} = \mu_v^{-1} + \left(\mu_\ell^{-1} - \mu_v^{-1}\right)H$$

$$k^{-1} = k_\ell^{-1}H,$$

$$H = 1 \qquad \text{if } \phi \geq +1.5h$$

$$= 0 \qquad \text{if } \phi \leq -1.5h$$

$$= 0.5 + \phi/(3h) + \sin\left[2\pi\phi/3h\right]/(2\pi) \qquad \text{if } |\phi| \leq 1.5h,$$

where h is a grid spacing. The step function, H, is smoothed over three grid spacings to prevent numerical instability arising from discontinuous material properties (refer to Sussman et al., 1994). The mass conservation equation, including the effect of volume expansion due to liquid–vapor change is derived from the conditions of the mass continuity and energy balance at the interface

$$m = \rho(u_{\text{int}} - u) = k\nabla T/h_{fg}, \tag{19}$$

$$\nabla\cdot u = -\frac{1}{\rho}\left(\frac{\partial\rho}{\partial t} + u\cdot\nabla\rho\right) + \dot{V}_{\text{micro}},$$

$$= \frac{m}{\rho^2}\cdot\nabla\rho + \dot{V}_{\text{micro}}. \tag{20}$$

In Eq. 20, $\dot{V}_{\text{micro}}$ has units of s^{-1} and is obtained from the microlayer solution as

$$\dot{V}_{\text{micro}} = \int_{R_0}^{R_1}\frac{k_l(T_W - T_{\text{int}})}{\rho_v h_{fg}\delta\Delta V_{\text{micro}}}r\,dr, \tag{21}$$

where ΔV_{micro} is a vapor-side control volume near the microregion, which was arbitrarily chosen to be $R_1 - 3h \le r \le R_1$ and $0 \le y \le h$. In the level-set formulation, the level-set function, ϕ, is advanced as

$$\frac{\partial \phi}{\partial t} = - u_{\text{int}} \cdot \nabla \phi, \tag{22}$$

and it is reinitialized as

$$\frac{\partial \phi}{\partial t} = \frac{\phi_0}{\sqrt{\phi_0^2 + h^2}} (1 - |\nabla \phi|), \tag{23}$$

where ϕ_0 is a solution of Eq. 22.

The boundary conditions for the governing equations for the macroregion are: at the wall ($y = 0$),

$$u = v = 0, \qquad T = T_W, \qquad \phi = -\cos \varphi; \tag{24}$$

at the planes of symmetry ($r = 0,\ R$),

$$u = \frac{\partial v}{\partial r} = \frac{\partial T}{\partial r} = \frac{\partial \phi}{\partial r} = 0; \tag{25}$$

at the top of the computational domain (free surface, $y = Y$),

$$\frac{\partial u}{\partial y} = \frac{\partial v}{\partial y} = \frac{\partial \phi}{\partial y} = 0; \qquad T = T_{\text{sat}}. \tag{26}$$

The procedure used to match asymptotically the solutions for the micro- and macroregions is as follows: (1) guess a contact angle; (2) solve the macroregion equations; (3) determine R_1 (radial location of the vapor–liquid interface at $y = h/2$); (4) solve the microlayer formulation with five boundary conditions for a given dispersion constant and determine R_0; (5) obtain the apparent contact angle from Eq. 16; and (6) repeat steps 1 to 5 if the contact angle obtained in step 5 is different from the guessed value in step 11.

Film Boiling. In stable film boiling, a vapor layer separates the liquid from the solid. The vapor from the interface during film boiling on a horizontal surface is removed from the interface as a result of three-dimensional Taylor instability. Figure 2a shows the vapor bubble release pattern as proposed by Sernas et al. (1973) for a surface with rectangular boundaries. The bubbles or valleys are spaced at a distance λ_{d_2} [$= 2\pi\sqrt{3\gamma/(\rho_\ell - \rho_v)g}$], and one bubble is released alternatingly from the node and antinode per $\lambda_{d_2}^2$ area of the heater during each half of the cycle. Recognizing the complexity of three-dimensional simulation, Son and Dhir (1997) carried out, as a first step, calculations in two-dimensional axisymmetric coordinates. As such, they chose two circular regions: one around the node, and another around the antinode. Each circular region (shown in Figure 2b) had an area equal to $\lambda_{d_2}^2/2$, with the origin located in the middle of the node and the antinode. With this geometry it was possible not only to describe the vapor bubbles as spherical rather than cylindrical but also to compute the alternate release of bubbles from the nodes and the antinodes. The computational domain is shown in Figure 2c. In describing the computational domain, the horizontal coordinate x is defined as

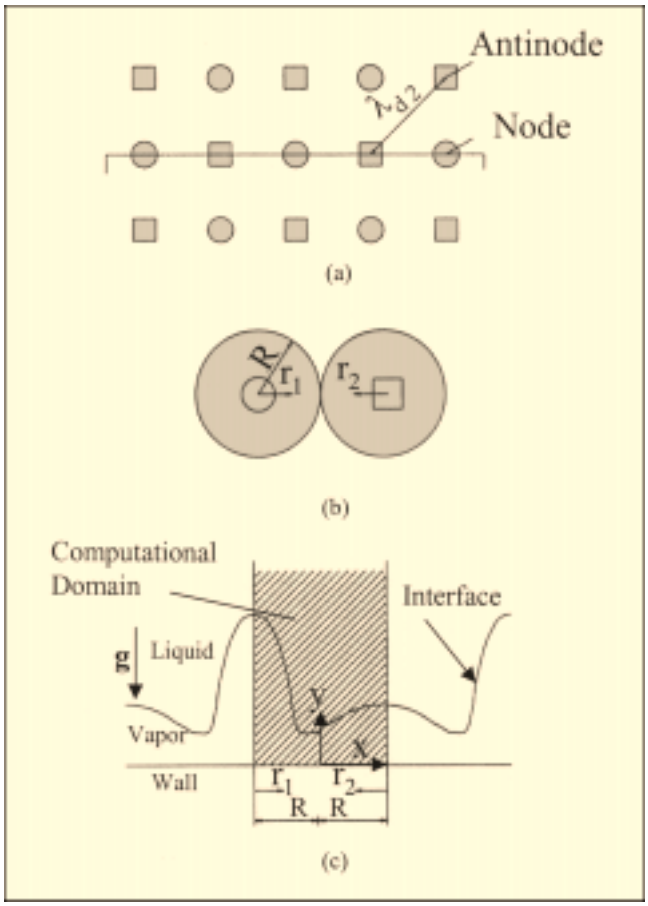

Figure 2. Two-circular regions used in numerical simulation for film boiling.

$$x = r_1 - R \qquad \text{for} \qquad 0 \le r_1 \le R$$
$$x = R - r_2 \qquad \text{for} \qquad 0 \le r_2 \le R,$$

where

$$R = \lambda_{d_2}/\sqrt{2\pi}.$$

In carrying out the numerical simulation, characteristic length, ℓ_0, characteristic time, t_0, and characteristic velocity, u_0, are defined

$$\ell_0 = \sqrt{\frac{\gamma}{g(\rho_\ell - \rho_v)}}; \qquad t_0 = \sqrt{\frac{\ell_0}{g}}; \qquad u_0 = \frac{\ell_0}{t_0}. \tag{27}$$

Also, vapor and liquid pressures are nondimensionalized with $\rho_v u_0^2$ and $\rho_\ell u_0^2$, respectively, and the dimensionless temperature is defined as

$$\theta = \frac{T_v - T_{\text{sat}}}{T_W - T_{\text{sat}}}. \tag{28}$$

In dimensionless form the equations governing the conservation of mass, momentum, and energy for vapor and liquid are written as

$$(ru)_x + (rv)_y = 0, \tag{29}$$

$$\frac{Du}{Dt} = -p_x + \frac{1}{\mathrm{Re}}\left(\nabla^2 u - \frac{u}{r^2}\right), \tag{30}$$

$$\frac{Dv}{Dt} = -p_y + \frac{1}{Re}\nabla^2 v, \tag{31}$$

$$\frac{D\theta}{Dt} = \frac{1}{\mathrm{PrRe}_v}\nabla^2\theta, \tag{32}$$

where p is a pressure modified to remove the body-force term in the momentum equation and for the general dependent variable ϕ, which represents dependent variables u, v, p, and θ

$$\frac{D\phi}{Dt} = \frac{\partial\phi}{\partial t} + u\frac{\partial\phi}{\partial x} + v\frac{\partial\phi}{\partial y}, \tag{33}$$

$$\nabla^2\phi = \frac{1}{r}\frac{\partial}{\partial x}\left(r\frac{\partial\phi}{\partial x}\right) + \frac{\partial^2\phi}{\partial y^2}, \tag{34}$$

also

$$\mathrm{Pr} = \frac{c_{pv}\mu_v}{k_v},$$

$$\mathrm{Re} = \mathrm{Re}_v = \frac{\rho_v u_0 \ell_0}{\mu_v} \qquad \text{for vapor,}$$

$$\mathrm{Re} = \mathrm{Re}_\ell = \frac{\rho_l u_0 \ell_0}{\mu_\ell} \qquad \text{for liquid.}$$

Since locally the thickness of the vapor film can be very small and significant distortion of the interface occurs at low pressure, Son and Dhir (1997) did not use the level-set method in a manner similar to that employed for nucleate boiling. Instead, they used coordinate transformation along with a staggered-grid system. Also, contravariant velocity components were used and while discretizing the governing equations temporally, the diffusion terms were treated by a fully implicit scheme. The convection, grid curvature, and source terms were treated by a first-order explicit method. In order to obtain a governing equation for pressure that achieved mass conservation, the fractional-step method or projection method was used.

The coordinates were transformed as

$$\xi = (x, y, t); \qquad \eta = (x, y, t).$$

With this transformation, the matching conditions for velocities and stresses at the interface are

$$u_\ell - u_v = -(1-\hat{\rho})\frac{y_\xi \dot{m}}{\sqrt{x_\xi^2 + y_\xi^2}} \tag{35}$$

$$v_\ell - v_v = -(1-\hat{\rho})\frac{x_\xi \dot{m}}{\sqrt{x_\xi^2 + y_\xi^2}} \tag{36}$$

$$\frac{1}{\hat{\mu}}\tau_\ell - \tau_v = 0 \tag{37}$$

$$\frac{1}{\hat{\rho}}p_\ell - p_v = \frac{1}{\mathrm{Re}_v}\left(\frac{1}{\hat{\pi}}\sigma_\ell - \sigma_v\right) + \frac{(1-\hat{\rho})}{\hat{\rho}}(y-\kappa) + (1-\hat{\rho})\dot{m}^2. \tag{38}$$

In the above equations

$$\hat{\rho} = \frac{\rho_v}{\rho_\ell}; \qquad \hat{\mu} = \frac{\mu_v}{\mu_\ell},$$

$$\dot{m} = \frac{c_{pv}\Delta T}{h_{fg}\mathrm{PrRe}_v}\frac{\sqrt{x_\xi^2 + y_\xi^2}}{J}\theta_\eta,$$

$$\tau = \frac{x_\xi^2 + y_\xi^2}{J}\frac{x_\xi u_\eta + y_\xi u_\eta}{x_\xi^2 + y_\xi^2} + \frac{x_\xi v_\xi - y_\xi u_\xi}{x_\xi^2 + y_\xi^2} - \frac{x_\xi x_\eta + y_\xi y_\eta}{J}\frac{x_\xi u_\xi + y_\xi v_\xi}{x_\xi^2 + y_\xi^2},$$

$$\sigma = -\frac{2u}{r} - \frac{2(x_\xi u_\xi + y_\xi v_\xi)}{x_\xi^2 + y_\xi^2},$$

$$\kappa = -\frac{x_\xi y_{\xi\xi} - y_\xi x_{\xi\xi}}{\left(x_\xi^2 + y_\xi^2\right)^{3/2}} - \frac{y_\xi}{r\sqrt{x_\xi^2 + y_\xi^2}},$$

and J is the Jacobian of transformation, $x_\xi y_\eta - x_\eta y_\xi$. Since the interface is maintained at saturation temperature

$$\theta = 0. \tag{39}$$

At the wall

$$u = v = 0; \qquad \theta = 1. \tag{40}$$

At the location of symmetry with respect to the y-axis

$$u = v_x = \theta_x = 0, \tag{41}$$

and far away from the interface

$$u_y = v_y = 0. \tag{42}$$

Banerjee and Dhir (2001a,b) have extended the numerical simulation model of Son and Dhir (1997) for saturated film boiling to the case when liquid is subcooled. In this case the dimensionless temperate in liquid is defined as

$$\theta_\ell = \frac{T_l - T_\infty}{T_{\mathrm{sat}} - T_\infty}. \tag{43}$$

This temperature is unity at the interface and is equal to zero far away from the interface. The rate of mass transfer across the interface includes that needed to support the heat loss to the subcooled liquid.

Son and Dhir (1998) have also studied film boiling near critical pressures. For this study they utilized the level-set method to understand the mechanism of the transition in vapor-release pattern with change in wall superheat. The governing equations and boundary conditions were similar to those employed for saturated film boiling at low pressures.

Experiments

In order to validate the results of numerical simulations, nucleate and film boiling experiments need to be performed under defined conditions. To investigate the dynamics of single and multiple bubbles without interference from extraneous sites, as may occur on a commercial surface, Qiu et al. (1999) used a polished silicon wafer as the test surface. The wafer was 10 cm in diameter and had a thickness of 1 mm. A cylindrical cavity 10 μm in diameter was etched on the surface using the deep RIE technique. Thin-film strain gage heaters were attached to the bottom surface of the wafer. Each strain gage heater had a heated area of 6.5 mm $\times$ 6.5 mm. By energizing the heaters individually, any number of cavities could be activated. Thermocouples were attached to the back side of the wafer to measure the temperature in the vicinity of the cavities. Figure 3 shows the test surface. A CCD camera was used to capture the boiling process. The camera could be operated up to a frame rate of 1020 frames/sec.

Saturated and subcooled film boiling on a horizontal disk has been studied by Banerjee and Dhir (2001b) using PF-5060 as the test liquid. In the experiments not only the rate of heat transfer, but also the bubble release pattern, bubble shape, and interface growth rate were measured.

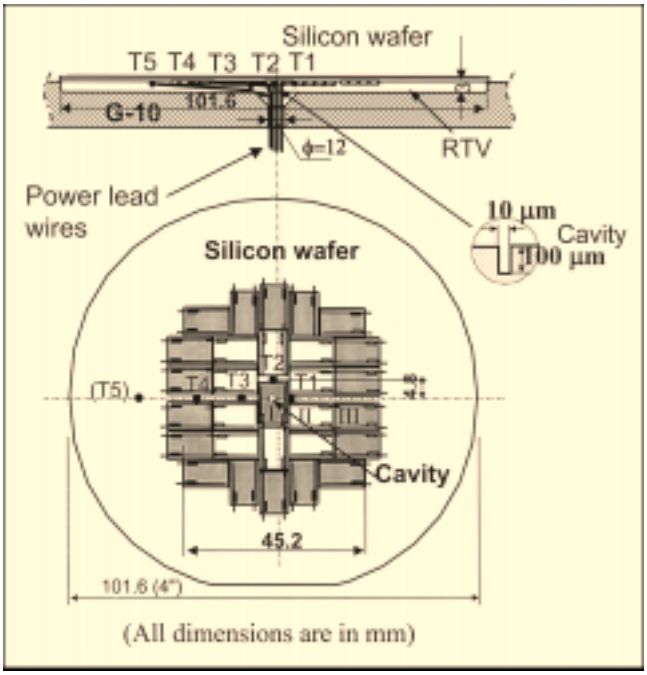

Figure 3. Configuration of silicon wafer heater.
All dimensions in mm.

Results and Discussion

The results of simulations of nucleate and film boiling are presented in this section and are compared with data from experiments. Only partial nucleate boiling and film boiling on a horizontal disk are considered.

Nucleate boiling

Since the numerical simulations were carried out under the assumption of axisymmetry, only single bubbles nucleating at a given site or bubble merge normal to the surface could be studied. In carrying out the simulations, the characteristic length l_0, the characteristic velocity u_0, and the characteristic time, t_0, as defined earlier, were used.

The computational domain was chosen to be $(R/\ell_0, Y/\ell_0) = (1,3)$ so that bubble growth is not affected by the computational boundary. Initially, turbulent natural convection is assumed to exist on the plate with the linear temperature profile in the boundary layer. The correlation used for the thermal boundary-layer thickness in turbulent natural convection is given as

$$\delta_\gamma = 7.14\left(\upsilon_\ell \alpha_\ell / g\,\beta_\gamma \Delta T\right)^{1/3}. \qquad (44)$$

Because the ebullition is a cyclic process, the computations need to be carried out over several cycles until no cycle-to-cycle change in the bubble growth pattern or in the temperature profile in the thermal layer is observed. The computational domain was divided into 96×288 grid points and a dimensionless time step of 5×10^{-4} was used.

Single-bubble dynamics and associated heat transfer

Figure 4 shows the computed bubble growth pattern during one cycle for $\Delta T = 6.2$ K and for the Hamakar constant

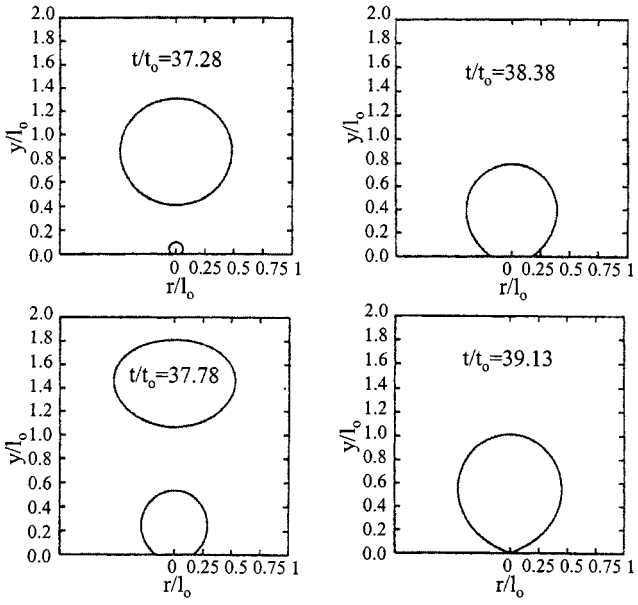

Figure 4. Bubble growth pattern for $\Delta T = 6.2$ K and $A = -8.5 \times 10^{21}$ J.

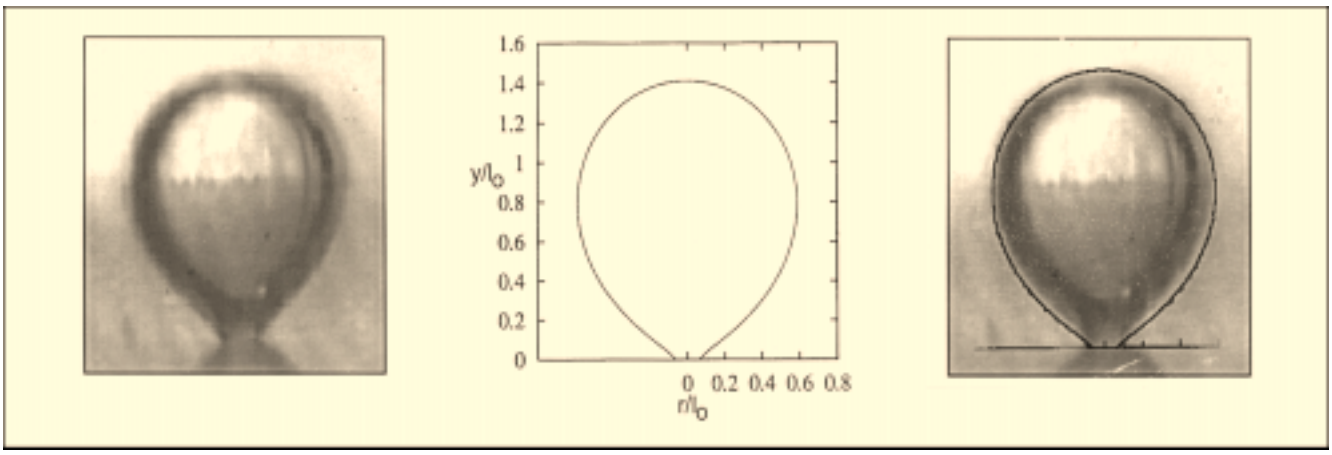

Figure 5. Prediction of bubble shape at departure with data for $\Delta T = 8.5$ K and $\varphi = 50°$.

$A = -8.5 \times 10^{-21}$ J. In obtaining the bubble growth pattern, the solution for the macroregion was coupled with the solution for the microregion, and an empirical relation was established between A and the apparent contact angle. However, the contact angle was assumed to remain constant in both the advancing and receding phases of the interface. As such, hysteresis of contact angle on a real surface was not modeled. It is seen from Figure 4 that during the early period of bubble growth $(37 \cdot 28 < t/t_0 < 38 \cdot 38)$ the location where the vapor–liquid interface contacts the solid wall moves radially outwards. However, the horizontal movement of the bubble base is retarded by the wall friction and the surface tension, forcing the bubble shape to satisfy the geometric condition (contact angle). This in turn tends to push the upper portion of the bubble outwards, and as a result leads to the increased buoyancy force. The nonuniform bubble motion introduces a clockwise vortex in the liquid layer. When the liquid vortex becomes stronger with the increase in the bubble diameter, the bubble base moves inwards $(38 \cdot 38 < t/t_0 < 39 \cdot 13)$. The departure process occurs rapidly because the dominance of buoyancy over surface tension force accelerates as the bubble base shrinks. In Figure 5 the bubble shape just prior to departure, obtained from the visual observations for a superheat of 8.5 K, is shown on the left and that obtained from the simulations, in the middle. On the right, the computed and observed shapes are overlayed. Overall the agreement between the two is quite good. However, some difference is observed in the neck region.

Since the bubble is not completely spherical, an equivalent diameter yielding a volume of a completely spherical bubble equal to that of the actual bubble was defined. In Figure 6 a comparison of the bubble diameter as a function of time predicted from the numerical simulations is made with the equivalent diameter obtained from the experiments. The predictions are for saturated water at one atmosphere pressure and for a wall superheat of 7 K. The static contact angle for water on silicon wafer was found to be about 50°. The advancing and the receding contact angle were found (Ramanujapu and Dhir, 1999) to vary within $\pm 5°$ of the static contact angle. From the empirical relationship between contact angle and the dispersion constant, A, the value of the dispersion constant for a contact angle of 50° was found to be -14.4×10^{-21} J. The predictions of bubble growth, bubble diameter at departure, and bubble growth time were found to be in good agreement with the data, except that the model tends to overpredict the growth period.

Although the temperature field in the vicinity of the bubble and the contribution of various mechanisms to heat transfer from the heater surface are difficult to determine in the experiments, the numerical simulations can provide such information. The temperature field around a bubble is shown in Figure 7. The crowding of the isotherms underneath the bubble is reflective of the very high flux in that region. Initially when a bubble is located inside the thermal boundary layer, the bubble grows as a result of evaporation all around the bubble interface including the microlayer. As the bubble grows out of the thermal layer, the energy required for evaporation is supplied through only the portion near the bubble base. It is also noted from the isotherms at $t/t_0 = 39.18$ that just after bubble detachment, a thin thermal layer forms over the area vacated by the departing bubble and the thickness of this thermal layer increases with time due to transient thermal conduction.

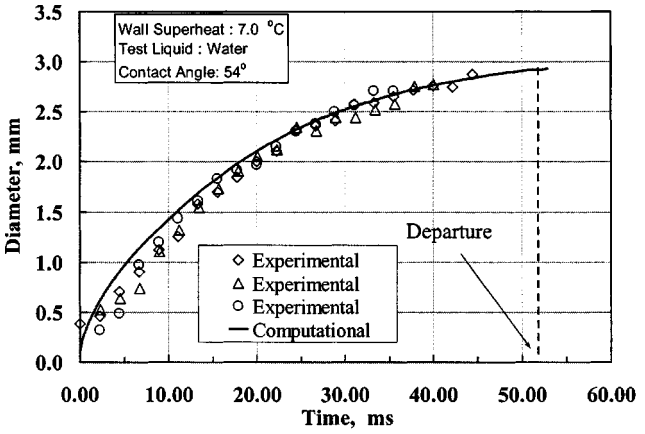

Figure 6. Bubble diameter predicted from numerical simulations with experimental data for $\Delta T = 7$ K and $\varphi = 50°$.

$A = -14.4 \times 10^{-21}$ J in simulations.

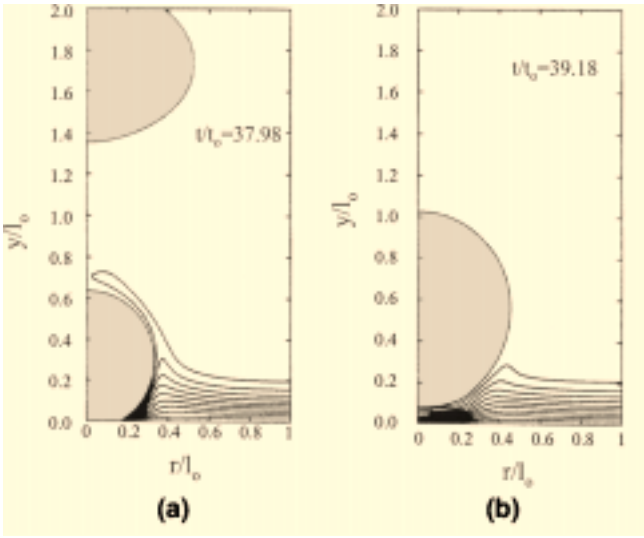

Figure 7. Temperature fields with temperature interval of 0.62 K for $\Delta T = 6.2$K and $A = -8.5 \times 10^{-21}$ J.

The temporal variation of the Nusselt number based on the area-averaged heat transfer coefficient at the wall, $\overline{Nu}$, and the local Nusselt number at the edge of the domain, $Nu_{r=R}$, as obtained from the numerical simulation, are plotted in Figure 8. Because of the uncertainty in the specification of the initial thickness of the thermal layer, the magnitude of the Nusselt number is seen to change from cycle to cycle. After about 14 cycles, however, quasi-steady-state conditions appear to have been achieved. The Nusselt number, Nu_{micro}, based on the contribution of the microlayer, is seen to be about 20% of $\overline{Nu}$, or, over the computational area, the heat transfer rate from the microlayer is about 20% of the total heat transfer rate from the heater surface.

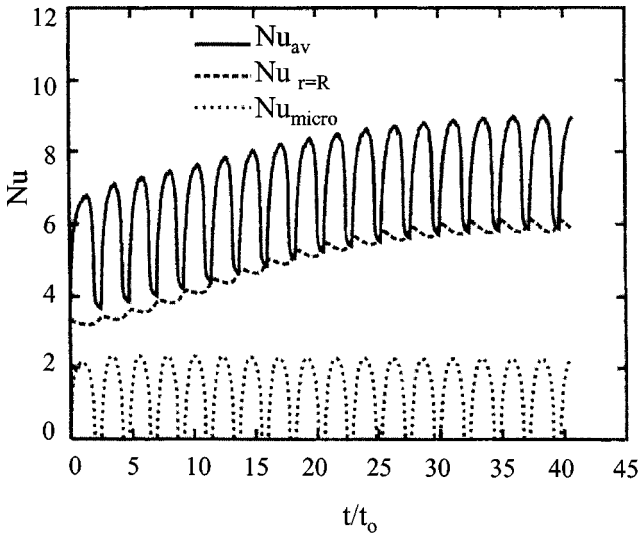

Figure 8. Variation of Nusselt number with time for various bubble growth cycles for $\Delta T = 6.2$ K and $A = -8.5 \times 10^{-21}$ J.

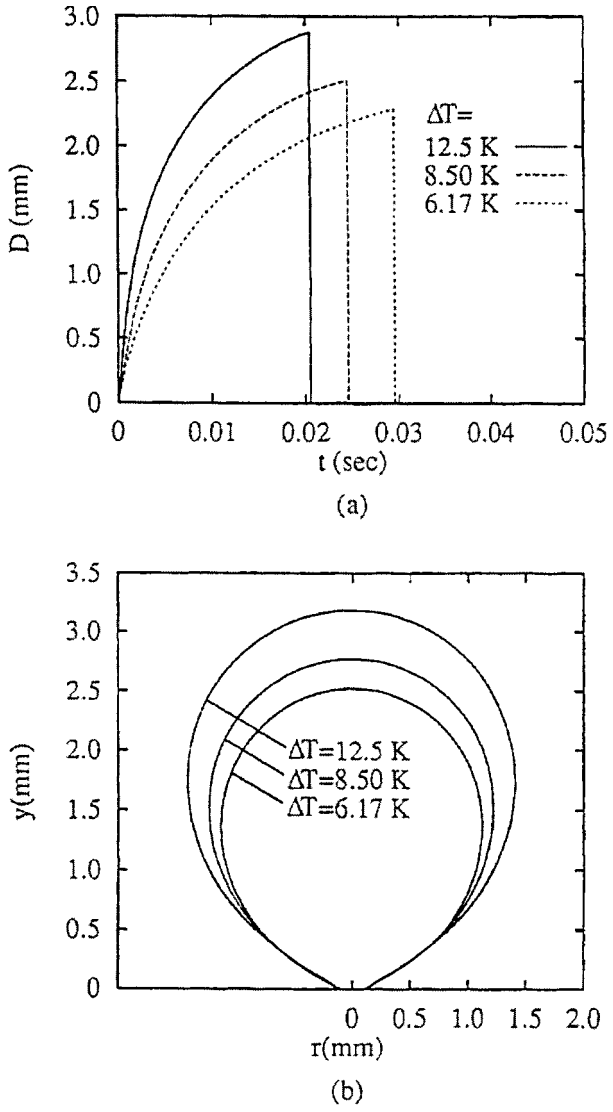

Figure 9. Effect of wall superheat (ΔT) on bubble growth.

Variation of bubble diameter with time and bubble shape at departure for $\varphi = 38$ deg.

Effect of Wall Superheat. Figure 9 shows, for different wall superheats, the bubble growth as obtained from numerical simulations carried out by Son et al. (1999). With an increase in the wall superheat, vapor-production rate or bubble growth rate increases. As a result, the growth period decreases. Also, the bubble diameter at departure increases with wall superheat. This indicates that for a fixed contact angle, the bubble diameter at departure depends on the growth rate, which increases with wall superheat. It should be noted that bubble diameter at departure is less sensitive to wall superheat than the growth period. The predictions from the numerical simulations are found to be consistent with data obtained from the experiments.

Effect of Contact Angle. The predicted dependence of bubble growth on the static contact angle is plotted in Figure

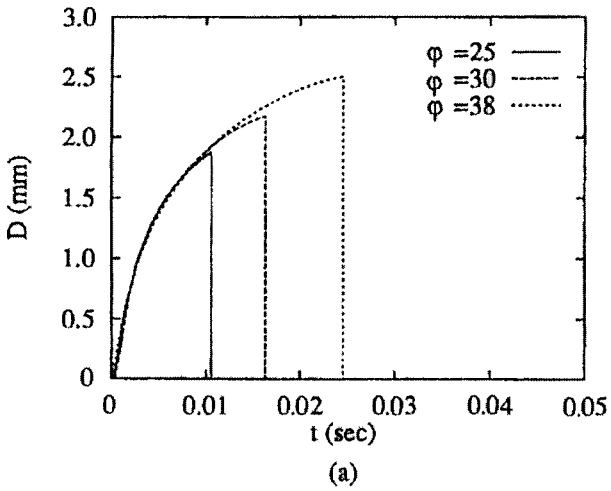

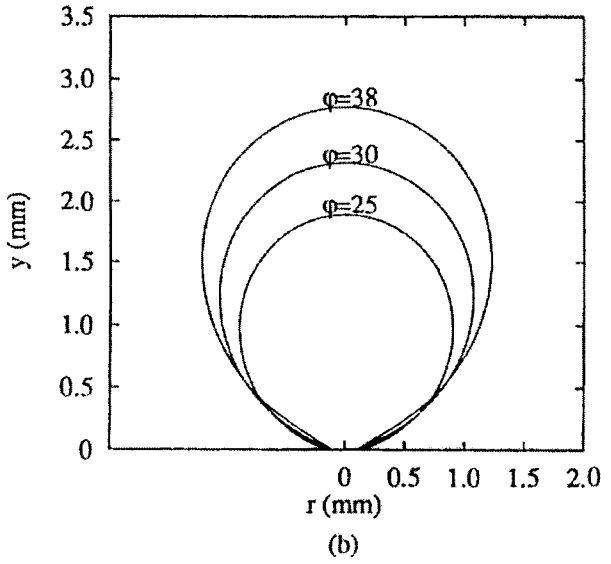

Figure 10. Effect on contact angle (φ) on bubble growth.

(a) Variation of bubble diameter with time; (b) bubble shape at departure for $\Delta T = 8.5$ K.

10. Computations were performed for contact angles of 25°, 30°, and 38°, which correspond to dispersion constants, A, of -3×10^{-21} (J), -5×10^{-21} (J) and -8.5×10^{-21} (J). As can be seen in Figure 10, as the contact angle increases, the bubble growth period increases. The bubble diameter at departure also increases. This is due to the fact that as the contribution of surface tension increases with the increase in contact angle, the vapor volume required for bubble departure also increases. The increase in bubble departure diameter with contact angle has been found to be in general agreement with the correlations proposed by Fritz (1935) and Staniszewski (1959).

Effect of Liquid Subcooling. When the liquid is subcooled, heat transfer to the liquid from the expanding interface of the bubble starts to play an important role. Figure 11 compares the bubble growth rate at a wall superheat of 8 K predicted for saturated water and for liquid subcoolings of 1 K and 2 K. It is noted that the effect of liquid subcooling is to reduce the bubble growth rate and to increase the bubble growth period. Reduced bubble growth occurs because of loss of vapor as a result of condensation on a portion of the vapor–liquid interface. The bubble diameter at departure also reduces with liquid subcooling, but the effect is small. The predicted trends are in agreement with data from experiments, except that growth periods are generally overpredicted.

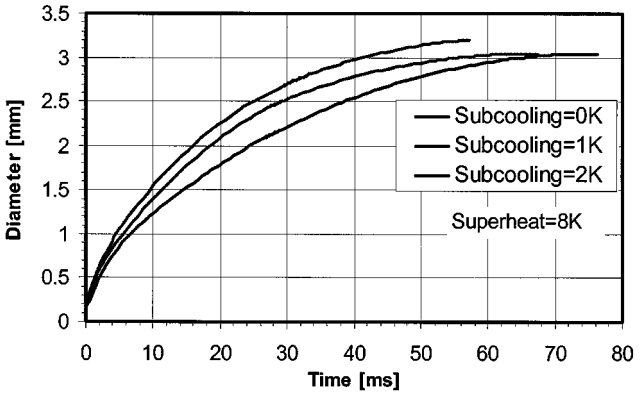

Figure 11. Bubble growth rates for $\Delta T = 8$ K, $\Delta T_{sub} = 1$ K, 2 K.

Isotherms in the liquid around the bubble for a subcooling of 1 K, are shown in Figure 12. Most of the evaporation occurs underneath the bubble and in the region below its equator, whereas condensation occurs in the region just above the equator. A plume of hot liquid is noted to form around the upper stagnation point. The total heat-transfer rate from the wall and the contributions of the microlayer, the evaporation around the bubble periphery, and condensation are plotted in Figure 13. Heat loss due to condensation of vapor is negligible during the early stages of bubble growth. However, in the later stages, as the interfacial area protruding into the subcooled liquid becomes large, the heat loss by condensation increases nearly linearly with time. As the bubble base shrinks, the heat loss by condensation just before bubble departure becomes almost equal to that due to evaporation.

Effect of Level of Gravity. The magnitude of gravitational acceleration is an important variable that can affect the bubble growth and departure process. The numerical simulations were also used to study the effect on bubble dynamics of the magnitude of gravitational acceleration normal to the heater surface. Figure 14 shows the predicted growth histories of single bubbles at gravity levels of $g/g_e = 1$, 10^{-2}, and 10^{-4} for saturated water at a wall superheat of 8° C, and for a contact angle of 50°. The last point in the growth histories represents the bubble departure diameter and the growth period. It is seen that at normal earth gravity the bubble grows to about 3.2 mm in diameter before departure, and the growth period is about 57 ms. The corresponding values for $g/g_e = 10^{-2}$ and $g/g_e = 10^{-4}$ are 2.9 cm and 5.5 sec, and 28 cm and 480 sec, respectively. Thus, it is seen that with reduction of gravity, both the bubble diameter at departure and the growth period increase. The bubble diameter at departure and the

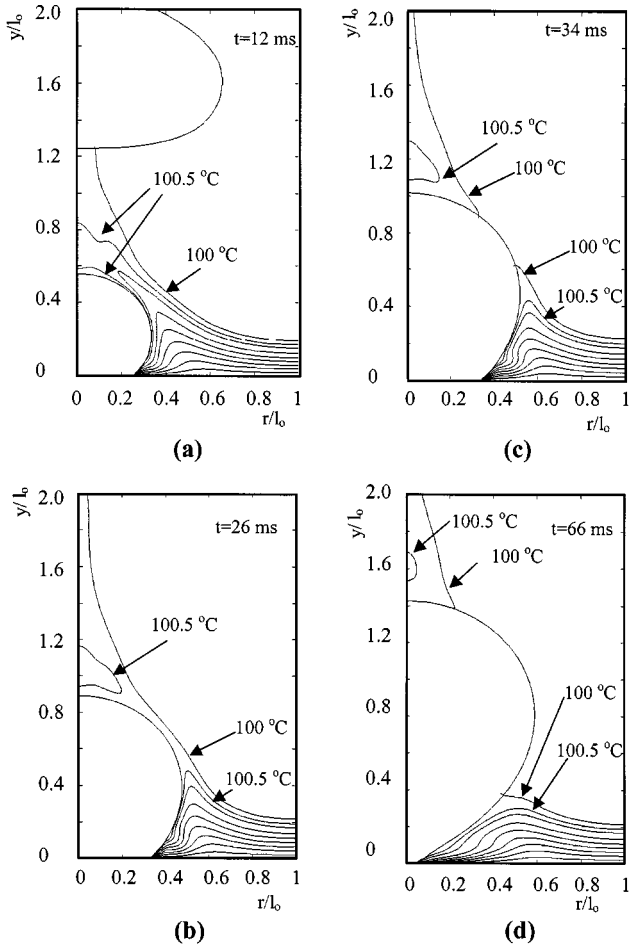

Figure 12. Temperature field for $\Delta T = 8$ K, $\Delta T_{sub} = 1$ K; isotherm interval = 1 K.

growth period are found to approximately scale with gravity as

$$D_g \sim g^{-1/2} \tag{45}$$

and

$$t_g \sim g^{-0.98}. \tag{46}$$

Predicted bubble size and shape at the moment when bubble base diameter reaches the maximum value are compared in Figure 15 with those of the bubble obtained in the low-gravity environment of the KC-135 aircraft (Qiu et al., 1999). The predicted and observed bubble shapes match quite well. However, the bubble base diameter appears to be slightly overpredicted. A comparison is made in Figure 16 of the predicted equivalent diameter of the bubble as a function of time with that obtained from the low-gravity experiments for both saturated and subcooled liquids. In both cases, the agreement between the data and model prediction is generally good. The model not only correctly predicts the bubble diameter at departure, but also the bubble growth period. In both cases the bubble diameter at departure is about the same, but with slight subcooling and lower wall superheat the growth period is increased by a factor of 3. Some deviations between prediction and data are seen for the subcooled liquid during the middle of the growth period. The differences are attributed to the directional change in the normal acceleration of the heater that occurred during the course of the parabolic flight of the KC-135 aircraft.

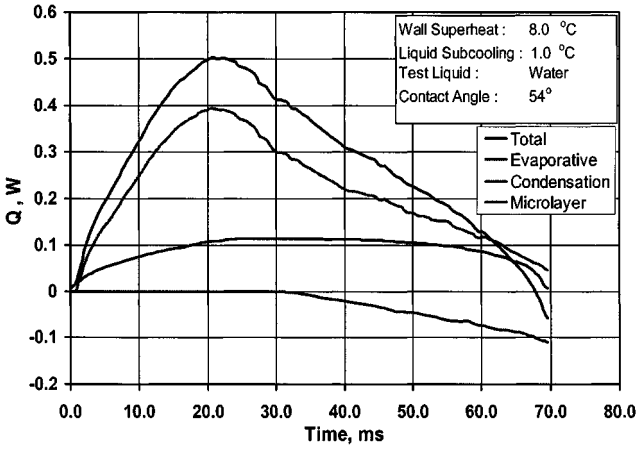

Figure 13. Distribution of the heat-transfer rate among various mechanisms for $\Delta T = 8$ K, $\Delta T_{sub} = 1$ K.

Heat Transfer in Partial Nucleate Boiling. Knowing the heat transfer over an area supporting a bubble and the nucleation site density from the mechanistic approach developed by Wang and Dhir (1993a,b), heat flux in partial nucleate boiling was predicted. Figure 17 compares the predicted dependence of heat flux on wall superheat with the data. The data are those given by Gaertner (1965). The agreement between the two is reasonable.

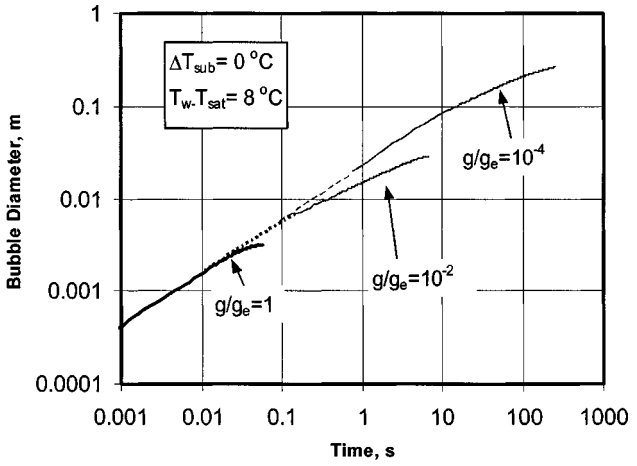

Figure 14. Numerical prediction of growth history of bubbles at gravity levels of $g_z/g_e = 1$, 10^{-2}, and 10^{-4} for saturated water at a wall superheat of 8°C.

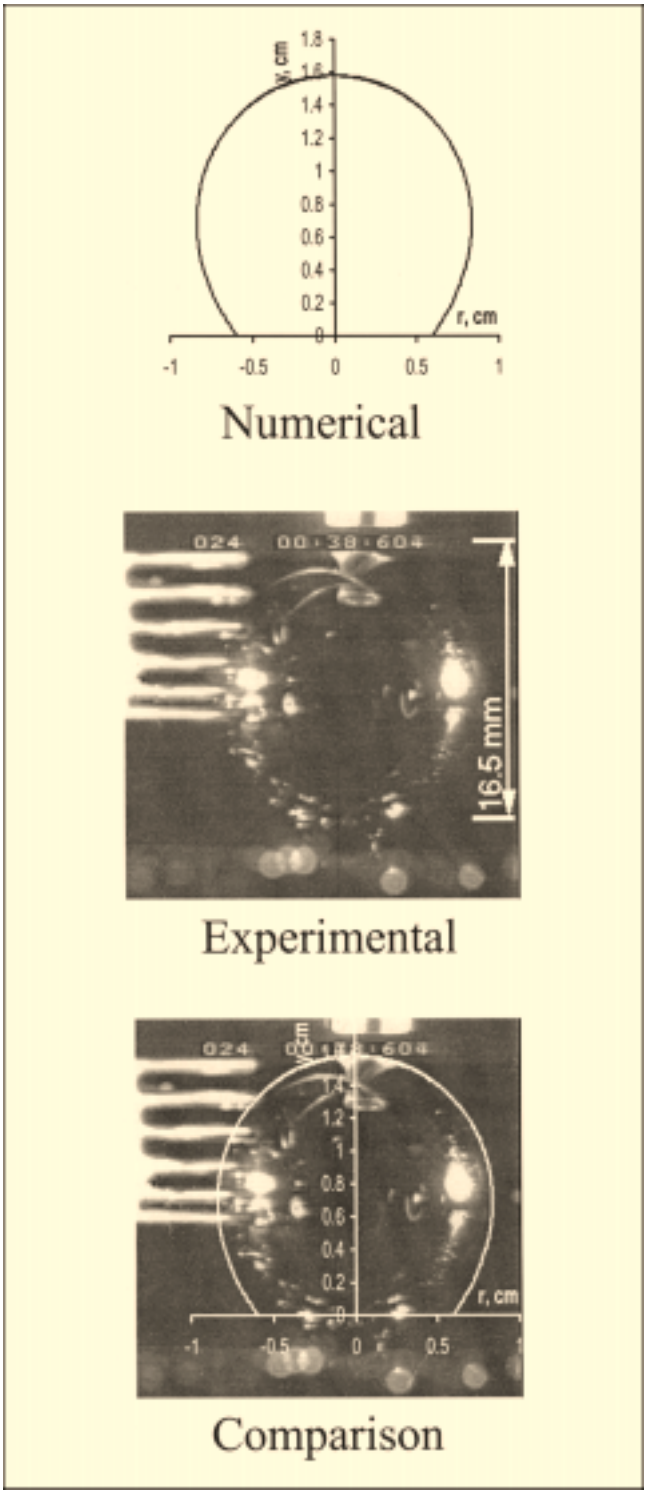

Figure 15. Measured and predicted bubble shapes at $T_W - T_S = 3.8°C$, $\Delta T_{sub} = 0.4°C$, and $g_z = 0.02\ g_e$.

Fully developed nucleate boiling

In fully developed nucleate boiling, the merger of vapor bubbles occurs both in the vertical as well as in the lateral direction. Since the axisymmetric model described earlier cannot handle bubble merger in the lateral direction, only the results of bubble merger in the vertical direction are described here.

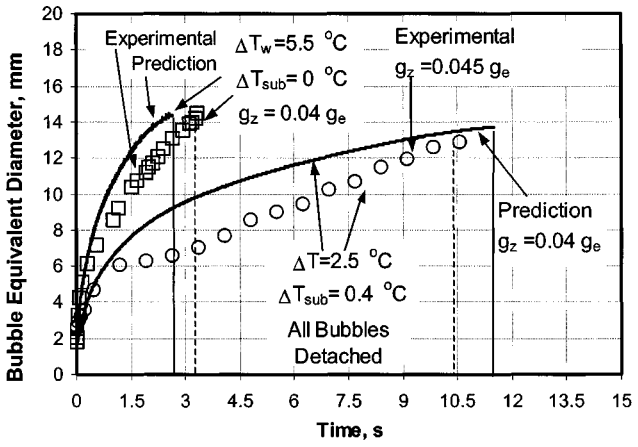

Figure 16. Measured and predicted bubble diameters, for saturated water and for subcooled water at low gravity.

Bubble Merger and Formation of Vapor Columns. The bubble merger in the vertical direction at a single nucleation site occurs when the growth rate of a bubble formed at the nucleation site exceeds the rate at which the lower interface of the preceding bubble moves away from the heater surface. After merger, the combined vapor mass may detach from the heater surface before the process repeats itself. Such a merger is referred to here as a two-bubble merger process. If, on the other hand, after merger the vapor mass merges with a second succeeding bubble before departure, we call it a three-bubble merger process. The shift from two- to three-bubble merger, and so on, depends on the wall superheat until vapor leaves the heater in almost continuous columns. Figure 18a and 18b show, respectively, the results of visual observations and those from numerical simulations for one cycle of the merger of three consecutive bubbles in the vertical direction.

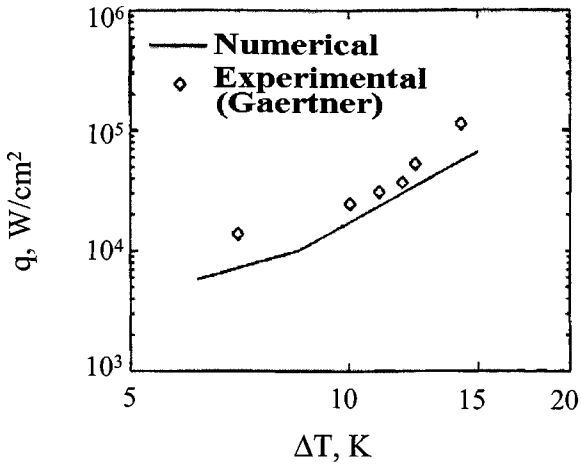

Figure 17. Partial nucleate boiling data with predictions from numerical simulations.

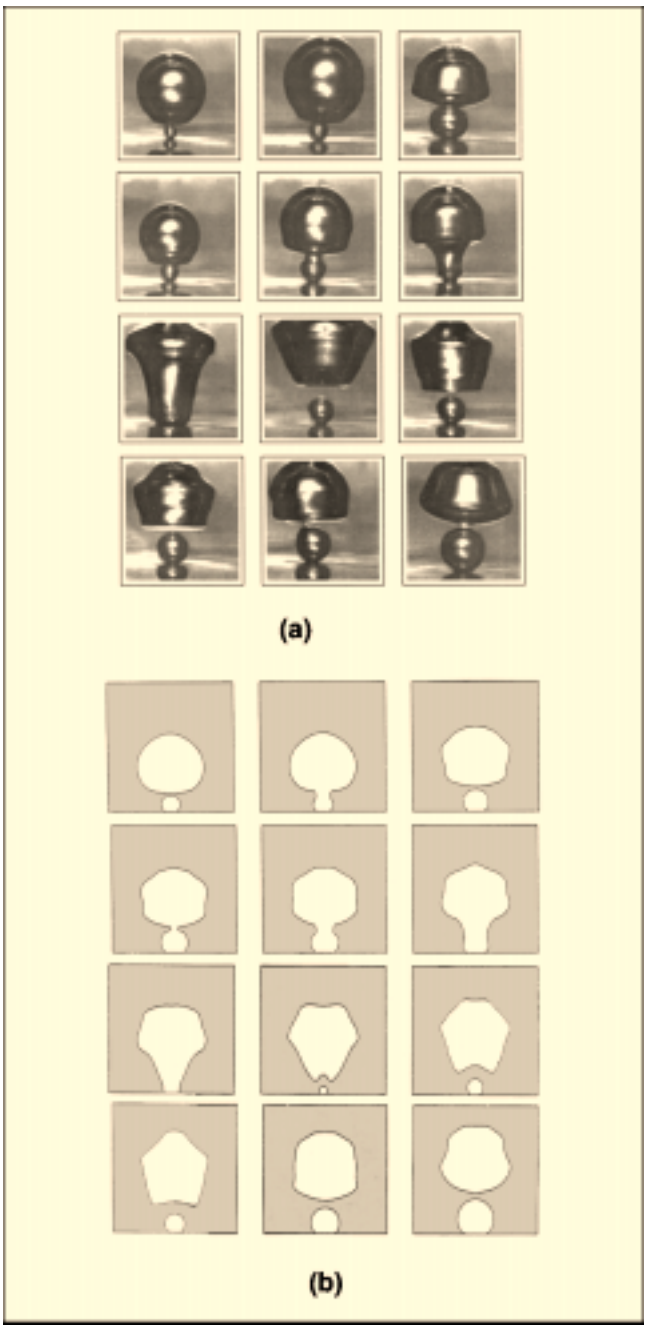

Figure 18. Bubble merger normal to the heater.

The individual frames in each figure are from left to right and from top to bottom. After the merger of the departed bubble with the succeeding bubble, the larger vapor mass causes the vapor bubble at the nucleation sites to prematurely depart. Thereafter, the second succeeding bubble merges with the vapor mass hovering over the surface. The combined vapor mass goes through several shape changes and departs as a cylindrical bubble. The departing bubble creates a wall jet that impinges on the lower interface of the bubble and forms a dimple. Thereafter, the vapor mass tries to acquire a spherical shape as it moves away from the wall. The rapid movement of the vapor mass breaks down the merger process before the cycle repeats itself. The bubble shapes as well as the merger behavior predicted from the numerical simulations is in startling agreement with the visual observations.

Film boiling

As stated earlier Son and Dhir (1997) used a coordinate transformation technique supplemented by a numerical-grid-generation method in their axisymmetric analysis of saturated film boiling at low pressures. Subsequently, Banerjee and Dhir (2000a, b) have extended this analysis to subcooled film boiling. Son and Dhir (1998) have also used the level-set method to investigate saturated film boiling at high pressures (near critical). In the following section, the main results from these studies are described.

Saturated Film Boiling at Low Pressures. Figure 19a shows at 1 atm pressure the calculated shapes of the evolving interface for $Ja_v^* = 0.09$ that corresponds to a wall superheat of 100 K for water. With the evolution of the interface (lefthand side), a neck starts to form. The location where the film is the thinnest moves radially inwards as the bubble evolves. The formation of the neck is governed by the reduced pressure that develops in the neck region as high-velocity vapor leaving the thinnest film region flows through the neck.

Figure 19b shows the dependence of the Nusselt number on the dimensionless time and dimensionless radial position for $Ja_v^* = 0.09$. Most of the heat is transferred in the thin-film region and in the bubble region in the vicinity of the point of the miminum film thickness. Little heat transfer takes place under the bubble core. The magnitude of the highest heat-transfer coefficient increases with time, and the location at which the film is the thinnest moves radially inward as the interface evolves into a bubble.

These observations run counter to Berenson's (1961) assumption of a uniform heat-transfer rate in the thin-film region connecting neighboring bubbles. The magnitude of the highest heat-transfer coefficient increases as the wall superheat or Ja_v^* decreases. Since the film is the thinnest where the heat-transfer rate is the highest, the magnitude of the minimum thickness decreases as wall superheat decreases. At a certain superheat, the film may become so thin that it ruptures. Any perturbations near the interface can accelerate the rupture process. Film rupture can lead to local liquid−solid contacts and can, in turn, cause the stable film boiling to cease. However, the exact nature of these contacts and the spreading behavior can be determined only if a conjugate problem involving conduction in the solid is solved simultaneously. This issue was not addressed in Son and Dhir's study (1997), but was subsequently investigated by Banerjee et al. (1996).

Figure 19c shows the Nusselt numbers based on the heat-transfer coefficient averaged over the cell area. With an increase in wall superheat, vapor film thickness in the thin-film region increases, and as a result, the heat-transfer coefficient decreases. The average Nusselt number also shows some dependence on time, but it is much less than that seen in the local heat-transfer coefficient. The Nusselt numbers based on the area- and time-averaged heat-transfer coefficients obtained by integrating the area under the curves (see Figure 19c) are about 30 to 35% lower than those obtained from

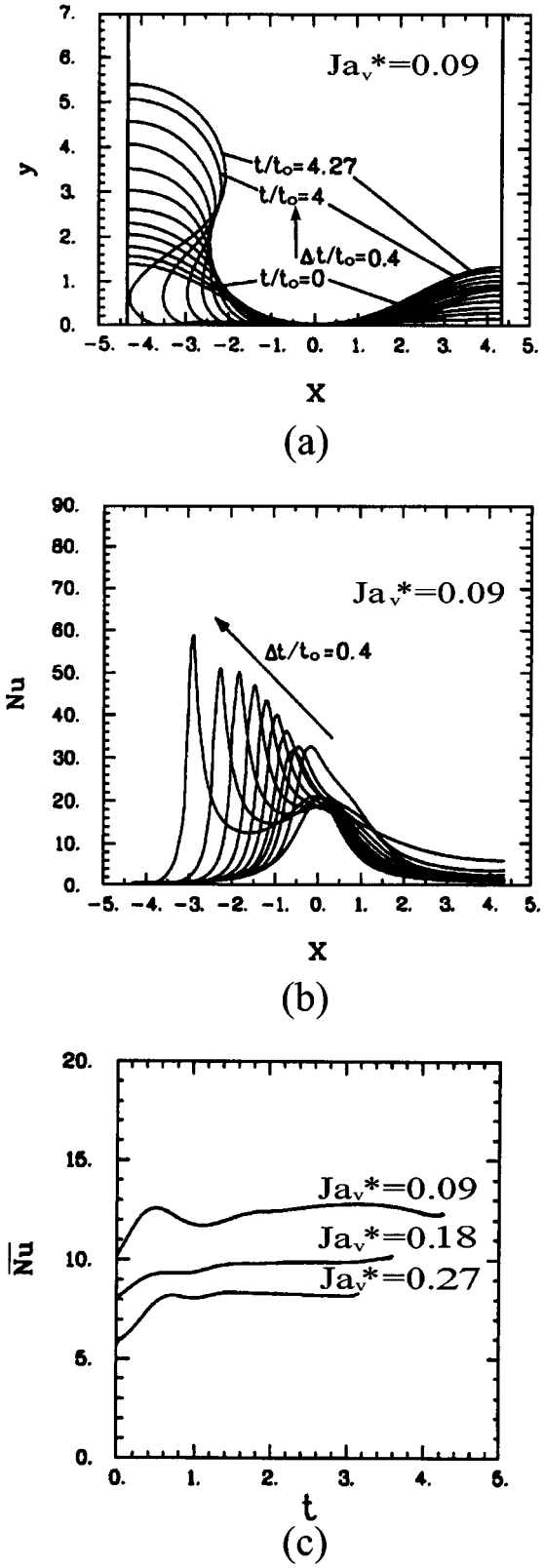

Figure 19. Prediction of film boiling on a horizontal surface.

(a) Evolution of the interface. (b) Heat-transfer coefficient as a function of position and time. (c) Nusselt number based on area-averaged heat-transfer coefficient.

Berenson's (1961) correlation. Also, the numerically calculated time- and area-averaged heat-transfer coefficients are closer to the lower bound of Hosler and Westwater's (1962) data. One possible reason for the underprediction of the heat-transfer rate from the numerical simulation is the use of axisymmetric analysis instead of three-dimensional analysis, which is more appropriate for low-pressure film boiling on a horizontal surface. It should be noted that numerical simulation results did not include thermal coupling with the solid.

Nevertheless, the analysis provides a better physical description of the film-boiling process on a horizontal surface. The numerical analysis, such as that used by Son and Dhir, can be a useful simulation tool for investigation of the effect of various system variables on the film-boiling process, including the thermal properties of the heater material.

Subcooled Film Boiling at Low Pressures. In contrast to saturated film boiling where liquid side heat transfer is nonexistent, in subcooled film boiling the liquid side heat transfer significantly affects the net evaporation at the interface and thereby influences the wall heat transfer. Figure 20 shows the various components of heat flux at the interface (Banerjee and Dhir, 2001a). The area-averaged heat flux at the wall, $\bar{q}_W$, is partitioned between the sensible heat gained by the vapor (area averaged), $\bar{q}_{vs}$, and the heat flux, $\bar{q}_{IV}$, at the interface (area averaged) from the vapor side. The heat fluxes are averaged over the cell area, which has a radius of $(\lambda_{d_2}/\sqrt{2\pi})$. The area-averaged heat flux at the interface from the vapor side, $\bar{q}_{IV}$, is partitioned between the area-averaged value of the heat lost to the liquid at the interface, $\bar{q}_{IL}$, and the heat flux, $\bar{q}_{VL}$, utilized for vapor production at the interface. Hence the total heat input, $\bar{q}_{VT}$, to the vapor phase per unit cell area is obtained by summing $\bar{q}_{VS}$ and $\bar{q}_{VL}$, or

$$\bar{q}_{VT} = \bar{q}_{VL} + \bar{q}_{VS}. \tag{47}$$

The corresponding Nusselt numbers are defined as

$$\overline{Nu}_w = \frac{\bar{q}_w \ell_0}{k_v \Delta T}$$

$$\overline{Nu}_{VT} = \frac{\bar{q}_{VT} \ell_0}{k_v \Delta T}$$

$$\overline{Nu}_{I,L} = \frac{\bar{q}_{I,L} \ell_0}{k_v \Delta T}$$

$$\overline{Nu}_{VL} = \frac{\bar{q}_{VL} \ell_0}{k_v \Delta T}$$

The bubble shapes obtained from numerical simulations for different liquid subcoolings are similar except that the effect of liquid subcooling is to reduce the bubble height as well as the sideways growth of the interface. At higher subcoolings, the liquid drag experienced by the vapor bubble is smaller because of the decrease in growth rate of the interface, and correspondingly there is less sideways protrusion of the vapor bubbles. Figure 21 compares the predicted and observed bubble shapes during film boiling of PF-5060 at one-atmosphere pressure. The liquid had a subcooling of 10 K and

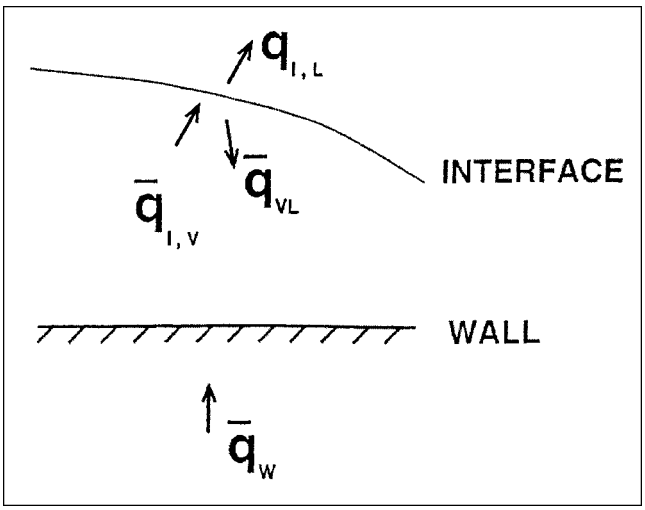

Figure 20. Various components of heat transfer at the interface and wall in subcooled film boiling.

wall superheat was 100 K. Three shapes prior to bubble departure are shown in Figure 21. The picture in the middle in each row was obtained from a single frame of the video motion picture recorded from the experiments. The bubble shape obtained from the numerical simulations is shown on the left of each row corresponding to a particular time step prior to bubble departure. On the righthand side, the predicted and observed bubble shapes are superposed. It is noted that the predicted interfacial shapes agree quite well with the experimental data.

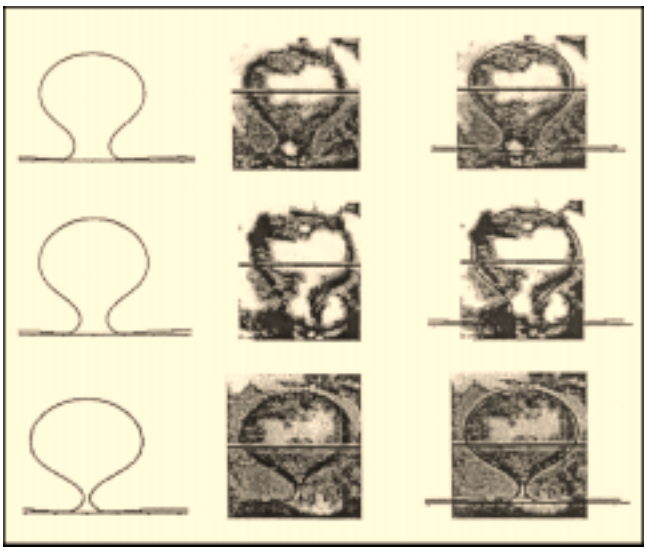

Figure 21. Vapor bubbles from experiments with numerical predictions for interface shape for subcooled film boiling of PF-5060 at a wall superheat of $\Delta T = 100$ K and $\Delta T_{sub} = 10$ K.

The pictures are at 1.2 ms intervals starting at 39.1 ms from the detected formation of the vapor bubble.

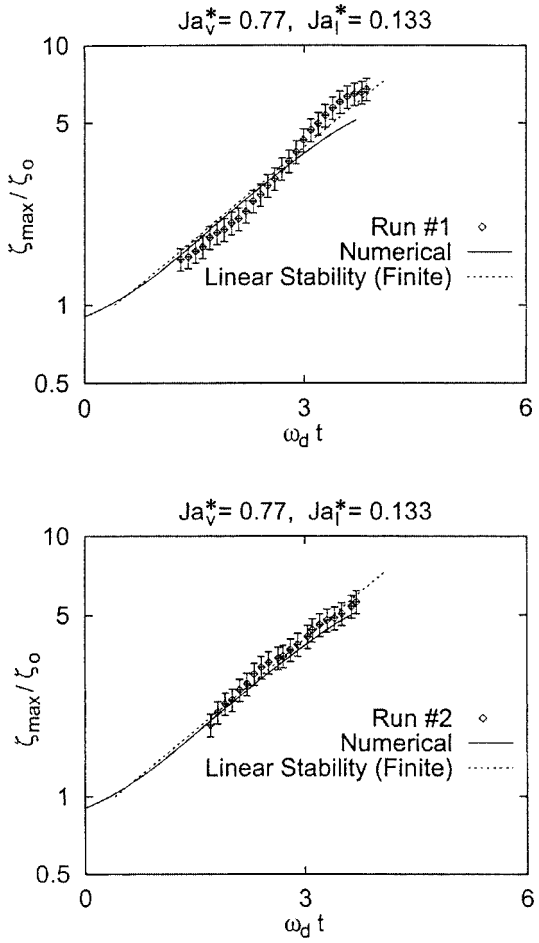

Figure 22. Experimental data with numerical predictions (solid lines) for temporal variation of bubble height for wall superheat, $\Delta T = 100$ K and liquid subcoolings, $\Delta T_{sub} = 10$ K.

The dotted line represents prediction from linear stability theory.

The highest position of the interface measured from the wall is plotted in Figure 22 for a subcooling of 10 K. The interface height is normalized with initial vapor-film thickness of 0.77 mm and time is normalized with respect to the inverse of the growth frequency obtained from linear stability analysis for infinite fluid layers. In these figures the solid line represents predictions from the numerical simulations, while the dotted line is from the linear stability theory. The last point on the solid line represents the peak height of the interface just before departure and at the end of the measured growth period. The numerical simulations correctly predict the nonlinear behavior of the interface during its evolution, especially the slowing down of the interface in the later stages of the growth period. The model generally tends to overpredict the maximum interface position just prior to bubble pinch-off by about 10%. However, in general, the observed growth periods lie within $\pm 10\%$ of the predictions.

The spatial variations of Nu_w at different times during the evolution of the interface for subcooled film boiling were found to be similar to those for saturated film boiling. How-

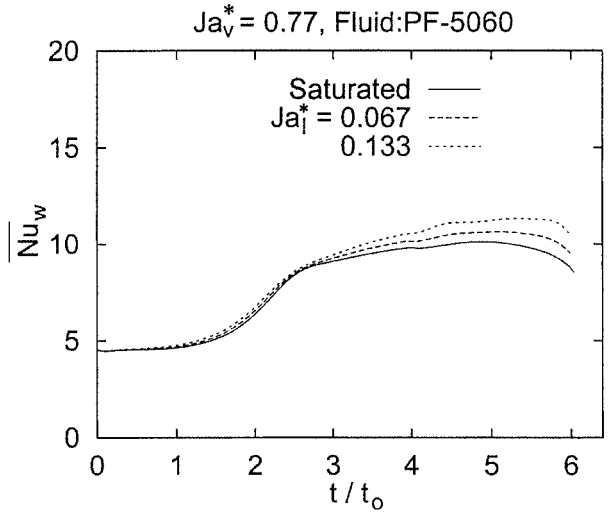

Figure 23. Temporal variation of area-averaged *Nu* at wall for wall superheat, $\Delta T = 100$ K and liquid subcooling, $\Delta T_{sub} = 5$ K and 10 K.

Time is nondimensionalized with respect to t_0.

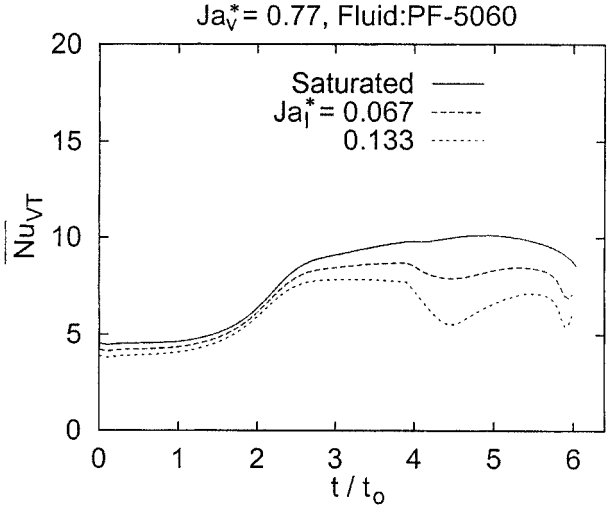

Figure 24. Temporal variation of component of area-averaged *Nu* in the vapor phase for wall superheat $\Delta T_W = 100$°C and liquid subcooling, $\Delta T_{sub} = 5$°C and 10°C.

Time is nondimensionalized with respect to t_0.

ever, the highest value of Nu_w tended to increase with increase in subcooling. Figure 23 shows the temporal variation of $\overline{Nu}_w$ computed for two subcoolings of PF-5060. It is noted that as the interface evolves a significant increase in $\overline{Nu}_w$ occurs from the initial value. The increase results from the increase in the local value of the heat-transfer coefficient in the thin-film region. With the increase in liquid subcooling the area-averaged heat-transfer coefficient increases. However, most of this enhancement occurs in the late stages of the evolution of the interface. In order to further understand the physics of the process, an area-averaged Nusselt number based on heat input into vapor (phase change and sensible heat) is plotted in Figure 24. It is seen that with the increase in liquid subcooling, less energy partitions into the vapor. The largest reduction in heat input into vapor occurs when the interfacial area of the evolving interface increases very rapidly. However, in the later stages of the evolution of the interface, some recovery in the total heat input into vapor takes place.

The Nusselt number based on area-averaged heat transfer into subcooled liquid (or $\overline{Nu}_{I,L}$) is plotted in Figure 25 as a function of time during the growth period of the interface. At a given time the Nusselt number increases as liquid subcooling is increased. For a given subcooling the Nusselt number remains fairly constant during the initial period, but increases very rapidly in the dimensionless time interval between 4 and 5. This is the period during which a rapid reduction in $\overline{Nu}_{VT}$ was observed. During the bubble growth period as much as a fivefold variation in the liquid side heat transfer is observed. Isotherms in the liquid show that during the period of rapid increase in interfacial area, the thermal boundary layer in the upper portion of the bubble thins and this in turn leads to an increase in the rate of heat transfer into liquid. However, in the later stages, as the interface slows down, the boundary layer thickens, once again reducing the rate of heat transfer into liquid.

In Figure 26 the Nusselt number based on the energy utilized in producing vapor at the interface is plotted as a function of radial position at different times during the evolution of the interface; negative values of the Nusselt number occur in the top portion of the vapor–liquid interface. The negative values imply that heat flux into liquid in the thin thermal-layer region is supported by the condensation of vapor. At a radial position of about 2, Nu_{VL} is shown to be multivalued. This is a reflection of the shape of the interface and simultaneous evaporation and condensation that occur on different parts

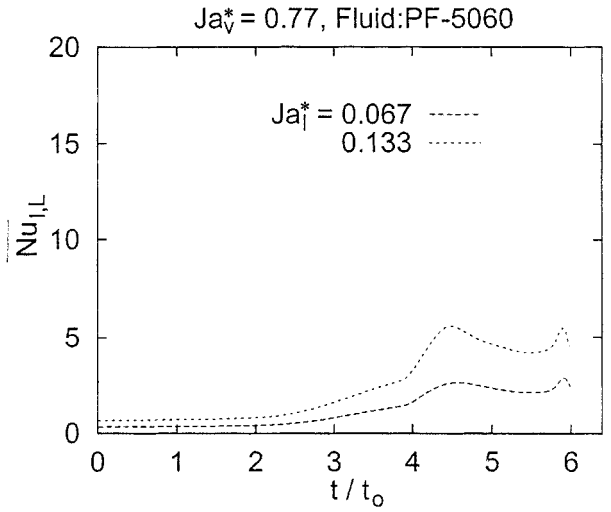

Figure 25. Temporal variation of component of area-averaged *Nu* in the liquid phase for wall superheat, $\Delta T_W = 100$°C and liquid subcooling, $\Delta t_{sub} = 5$°C and 10°C.

Time is nondimensionalized with respect to t_0.

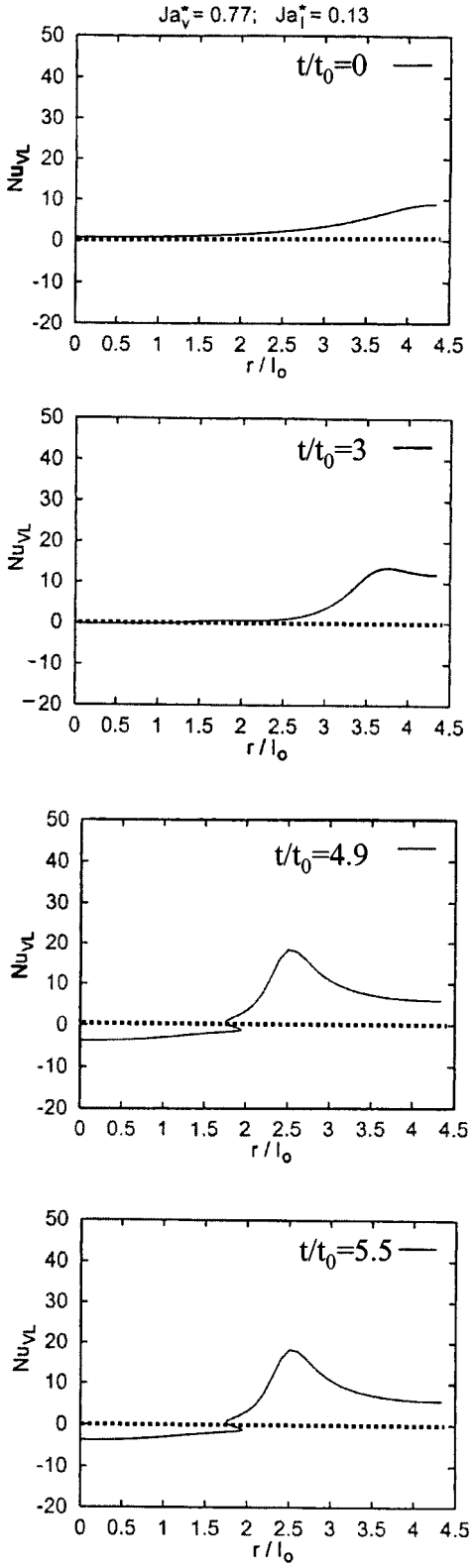

Figure 26. Local *Nu* at interface for latent heat transfer into the vapor bubble for $t = 0, 3, 4.9$, and 5.5.

Time is nondimensionalized with respect to t_0, and radial distance is nondimensionalized with respect to l_0.

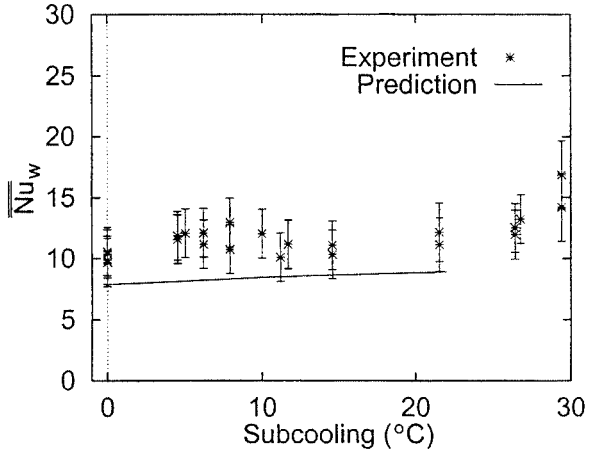

Figure 27. Predictions for $\overline{\overline{Nu}}_w$ with experimental data for wall superheat, $\Delta T_W = 100°C$, and liquid subcooling up to $\Delta T_{sub} = 22°C$.

Time is nondimensionalized with respect to t_0.

of the interface. The maximum value of Nu_{VL} occurs at the location where film is the thinnest.

A comparison of the Nusselt numbers based on the area- and time-averaged heat-transfer coefficients measured in the experiments is made with predictions from numerical simulations in Figure 27. It should be noted that numerical simulations were made for a constant heater surface temperature, whereas the experiments were conducted by controlling the wall heat flux. It has been shown by Banerjee et al. (1996) that because of spatial and temporal variations in the total heat-transfer coefficient, local heater surface temperature varies with time. For a thick copper surface, however, the temperature variations are not expected to be significant, and in turn the difference in the predicted heat-transfer coefficient for constant wall temperature and that for constant heat flux cases is expected to be quite small. From Figure 27 it is found that predictions for PF-5060 are about 20% lower than the best fit through the data. Two possible reasons are advanced for this underprediction. The first is the same as for saturated film boiling discussed earlier in that numerical simulations are based on a two-dimensional axisymmetric model for the film-boiling process. In reality the process is three-dimensional. The second reason is the uncertainty that exists in thermophysical properties in PF-5060 vapor, especially thermal conductivity and viscosity.

Saturated Film Boiling at High Pressures. At pressures near critical pressure, a transition in the vapor bubble release pattern occurs. By using the level-set method, Son and Dhir (1998) investigated the bubble-release-pattern-associated heat transfer during saturated film boiling of water near the critical pressure. Figure 28 shows the evolution of the vapor–liquid interface for different wall superheats of $T_{sat} = 646.4$ K. The corresponding saturation pressure is 21.90 Mpa, which is 0.99 times the critical pressure for water. It is found in Figure 28a that at the low wall superheat, $\Delta T = 10$ K, discrete vapor bubbles are released alternatively at the nodes and antinodes, like film boiling at low pressures. After the vapor bubble pinches off, a part of the vapor stem also breaks off as shown at $t/t_0 = 157$ and $t/t_0 = 164$. Such a breakoff leads

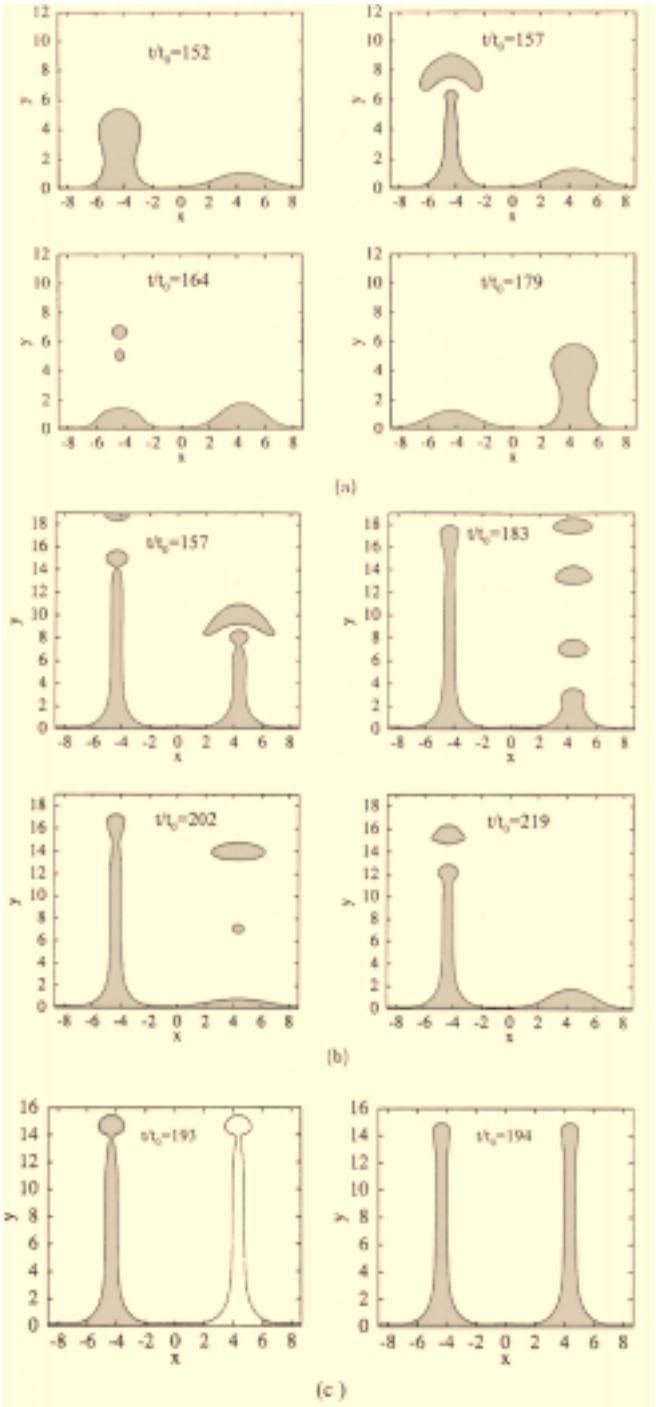

Figure 28. Evolution of the interface for different wall superheats at T_{sat} = 373.3°C: (a) ΔT = 10°C, (b) ΔT = 22°C, and (c) ΔT = 30°C.

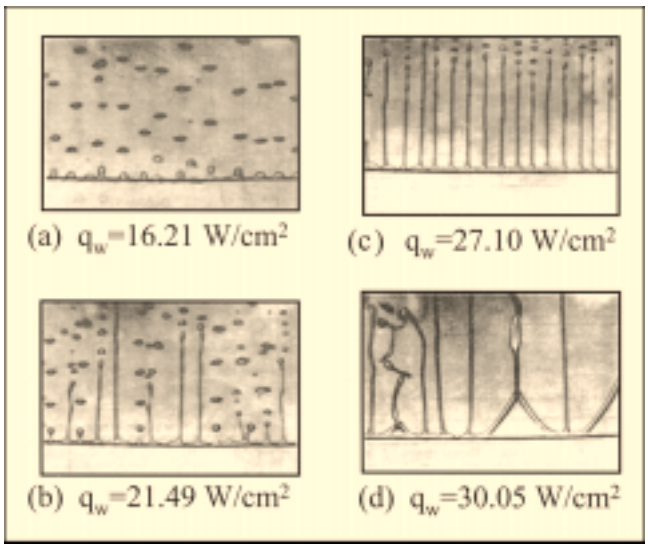

Figure 29. Hydrodynamic transition in bubble release pattern.

Observed by Reimann and Grigull (1975) and presented in the article of Dhir and Taghavi-Tafreshi (1981).

to the formation of small secondary bubbles. After bubble breakoff, the interface in the peak region rapidly drops down because of the restoring force of surface tension. When the wall superheat is increased to $\Delta T = 22$ K, the bubble release pattern changes, as shown in Figure 28b. A stable vapor jet forms on the node ($x = -R$), while the pattern of discrete bubble release still exists on the antinode ($x = R$). At a higher superheat, $\Delta T = 30$ K, stable jets are formed on both the node and antinode. Figure 28c shows that the interface is nearly stationary, except for the fact that bubbles are released from the upper end of the vapor columns. Also, at the nearly steady-state condition, the interface is found to be almost symmetric with respect to $x = 0$. These hydrodynamic transitions in bubble release pattern are consistent with those observed by Reimann and Grigull (1975). These authors observed that during film boiling of water on 0.1-mm diameter platinum wire at $T_{sat} = 646.4$ K, vapor left in several different modes, as shown in Figure 29. With an increase in heat flux, the modes of vapor removal shift from (a) to (d). Modes (a), (b), and (c) are similar to the bubble release pattern simulated numerically in the present study. It is interesting to note that the heat fluxes for Figure 29b and 29c are comparable to the heat fluxes $q_w = 29.9$ (W/cm^2) obtained numerically for different bubble release modes, though the geometry of boiling surface is not the same.

In contrast with low pressures, at a pressure near the critical, the Nusselt number based on the area- and time-averaged heat-transfer coefficients is found to slightly increase with wall superheat of Ja_v^*. This increase results from the fact that the formation of stable vapor jets at high wall superheats increases the pressure difference between the peak and the valley region of the interface, which provides more efficient flow passage for vapor removal.

The numerical simulations of film boiling at high pressures, as well as at low pressures, provide a completely theoretical basis for correlation of the Nusselt number for film boiling on a horizontal surface. The range of parameters varied during the computations is as follows

$$Gr = 210 \sim 2.2\times10^6, \qquad \mathrm{Pr} = 0.72 \sim 420,$$
$$Ja_v^* = 0.09 \sim 140.$$

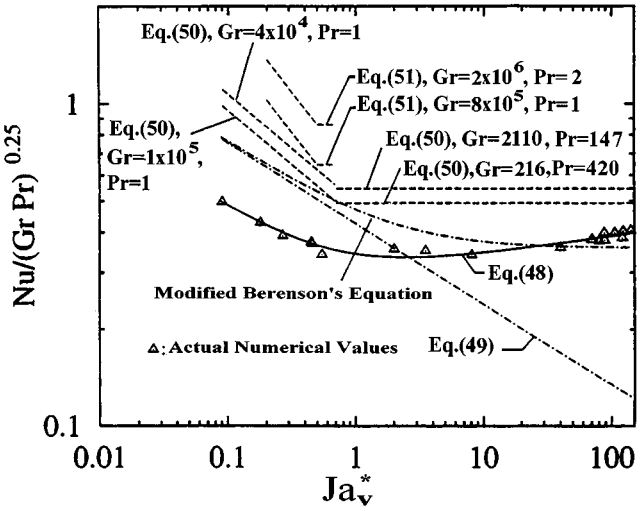

Figure 30. Correlation of the Nusselt number obtained from the numerical simulations.

Effect of radiation has not been included.

The Nusselt numbers obtained numerically are fitted within at most a ± 6 percent deviation with the following equation

$$Nu = 0.265(Gr\ \mathrm{Pr})^{1/4}. \qquad \left(Ja_v^{*-1} + 0.5 + 1.3\,Ja_v^{*0.25}\right)^{1/4}. \tag{48}$$

In Eq. 48 the contribution of radiation was not included. Therefore, the correlation is valid as long as T_w is less than 673.15 K and emissivity of the surface is relatively small. The predictions from Eq. 48 are plotted in Figure 30. It is seen that for low Ja_v^* corresponding to low pressures, the Nusselt numbers vary as $Ja_v^{*-1/4}$, which is consistent with Berenson's prediction (even though the Nusselt numbers obtained from the numerical simulations are about 34 percent lower than those obtained from Berenson's static model). However, for high Ja_v^* the Nusselt numbers predicted numerically increase slightly with Ja_v^*, unlike Berenson's prediction. It is noted that this correlation of Nusselt number for film boiling was obtained from purely numerical simulations, even though the computations were restricted to two-dimensional cases. Furthermore, near critical pressures, the cell fractional area occupied by an evolving vapor bubble or a vapor column is much smaller than that for an evolving vapor bubble during film boiling at low pressures. This, in turn, casues the film boiling near critical pressures to be closer to a two-dimensional (axisymmetric) situation than is flim boiling at low pressures. In Figure 30, Berenson's (1961) correlation is given by

$$\overline{\overline{Nu}}_B = 0.425(Gr\ \mathrm{Pr}/Ja_v^*)^{1/4} \tag{49}$$

while in the modified form of the preceding equation, correction for sensible heating of the vapor is made by replacing Ja_v^* by $Ja_v^*/(1+0.5\ Ja_v^*)$. Klimenko's (1981) correlation is written as

$$\overline{\overline{Nu}}_k = 1.90\times 10^{-1} Gr^{1/3}\mathrm{Pr}^{1/3} f_1; \qquad \text{for} \qquad Gr < 4.03\times 10^5 \tag{50}$$

$$\overline{\overline{Nu}}_k = 2.16\times 10^{-2} Gr^{1/2}\mathrm{Pr}^{1/3} f_2; \qquad \text{for} \qquad Gr > 4.03\times 10^5 \tag{51}$$

where

$$f_1 = 1 \quad \text{for} \quad Ja_v^* > 0.71$$
$$= 0.89\,Ja_v^{*-1/3} \quad \text{for} \quad Ja_v^* < 0.71,$$
$$f_2 = 1 \quad \text{for} \quad Ja_v^* > 0.50$$
$$= 0.71\,Ja_v^{*-1/2} \quad \text{for} \quad Ja_v^* < 0.50,$$

Conclusions

- Numerical simulations of evolving liquid–vapor interfaces during a phase-change process such as boiling have been shown to provide significant additional insights into the phenomena.
- Numerical simulations can be used as an effective tool for the study of the effect of various system variables. However, they are not a substitute for detailed experiments, the results of which are needed to validate the simulations.
- Numerical simulations employed in this work have been two-dimensional. These need to be extended to three dimensions to eliminate the restrictions imposed by two-dimensional solutions.
- In the future, numerical simulations such as those described in this work, would become routine and will be an integral part of the research activity in phase-change heat transfer.

Acknowledgments

This work received support from NASA under the Microgravity Fluid Physics Program.

Notation

A = dispersion constant
c_p = specific heat at constant pressure
D = bubble diameter
D_c = cavity diameter
D_d = bubble diameter at departure
Gr = Grashof number, $(g\beta_T \Delta T \ell_0^3)/(\nu^2)$
g = gravity vector
H = step function
h = grid spacing for the macroregion
h_{ev} = evaporative heat-transfer coefficient
h_{fg} = latent heat of evaporation
Ja_ℓ^* = liquid subcooling parameter, $c_{p\ell}\Delta T_{\mathrm{sub}}/h_{fg}$
Ja_v^* = vapor superheat parameter, $c_{pv}\Delta T/h_{fg}$
k = thermal conductivity
ℓ_0 = characteristic length, $\sqrt{\gamma/g(\rho_\ell - \rho_v)}$
M = molecular weight
m = mass flux vector
Na = number density of active sites
Nu = Nusselt number, $l_0 q/k\Delta T$
p = pressure
q = heat flux
R = radius of computational domain
$\overline{R}$ = universal gas constant
R_0 = radius of dry region beneath a bubble
R_1 = radial location of the interface at $y = h/2$
r = radial coordinate

T = temperature
ΔT = temperature difference, $T_w - T_{\text{sat}}$
ΔT_{sub} = liquid subcooling, $T_{\text{sat}} - T_l$
t = time
t_0 = characteristic time, $\ell_0 u_0$
t_w = waiting time
u = r-directional velocity
u = velocity vector, (u,v)
u_{int} = interfacial velocity vector
u_0 = characteristic velocity, $\sqrt{g\,\ell_0}$
$\dot{V}_{\text{micro}}$ = rate of vapor volume production from the microlayer
ΔV_{micro} = control volume near the microregion
v = y-directional velocity
x = horizontal coordinate
Y = height of computational domain
y = vertical coordinate

Greek letters

α = thermal diffusivity
β_γ = coefficient of thermal expansion
δ = liquid film thickness
δ_γ = thermal layer thickness
θ_ℓ = dimensionless temperature, $(T - T_\infty)(T_{sat} - T_\infty)$
γ = surface tension
κ = interfacial curvature
μ = dynamic viscosity
ν = kinematic viscosity
ρ = density
ϕ = level set function
φ = contact angle

Subscripts and superscripts

g = growth
int = interface
ℓ, v = liquid, vapor
$r, y, t, =$ $\partial/\partial r$, $\partial/\partial y$, $\partial/\partial t$
sat, w = saturation, wall
$\bar{}$ = area average
$\bar{\bar{}}$ = area and time averaged

Literature Cited

Banergjee, D., and V. K. Dhir, ''Study of Subcooled Film Boiling on a Horizontal Disc: I. Analysis,'' *J. Heat Transfer*, 123 (2001a).

Banerjee, D., and V. K. Dhir, ''Study of Subcooled Film Boiling on a Horizontal Disc: II. Experiments,'' *J. Heat Transfer*, 123 (2001b).

Banerjee, D., G. Son, and V. K. Dhir, ''Conjugate Thermal and Hydrodynamic Analysis of Saturated Film Boiling from a Horizontal Surface,'' ASME Meeting, Atlanta, GA (1996).

Bankoff, S. G., ''Entrapment of Gas in the Spreading of Liquid over a Rough Surface,'' *AIChE J.*, **4**, 24 (1958).

Berenson, P. J., ''Film Boiling Heat Transfer from a Horizontal Surface,'' *J. Heat Transfer*, **83**, 351 (1961).

Breen, B. P., and J. W. Westwater, ''Effect of Diameter of Horizontal Tubes on Film Boiling Heat Transfer,'' *Chem. Eng. Prog. Symp. Ser.*, **58**, 67 (1962).

Bromley, C. A., ''Heat Transfer in Stable Film Boiling,'' *Chem. Eng. Prog. Symp. Ser.*, **46**, 221 (1950).

Buyevich, Y. A., and B. W. Webber, ''Towards a New Theory of Nucleate Pool Boiling,'' Eur. Thermal Sciences Conf., Rome, Italy (1996).

Cole, R., and W. Rohsenow, ''Correlations of Bubble Departure Diameters for Boiling of Saturated Liquids,'' *Chem. Eng. Prog.*, **65**, 211 (1969).

Cooper, M. G., ''Heat Flow Rates in Saturated Nucleate Pool Boiling—A Wide Ranging Examination Using Reduced Properties,'' *Adv. Heat Transfer*, **16**, 155 (1984a).

Cooper, M. G., ''Saturation Nucleate Boiling—A Simple Correlation,'' *Int. Chem. Engineering Symp. Ser.*, **86**, 276 (1984b).

Cooper, M. G., A. M. Judd, and R. A. Pike, ''Shape and Departure of Single Bubbles Growing at a Wall,'' *Proc. Int. Heat Transfer Conf.*, Toronto, Canada, Vol. 1, p. 115 (1978).

Cooper, M. G., and A. J. P. Lloyd, ''The Microlayer in Nucleate Pool Boiling,'' *Int. J. Heat Mass Transfer*, **12**, 895 (1969).

Fritz, W., ''Maximum Volume of Vapor Bubbles,'' *Phys. Z.*, **36**, 879 (1935).

Gaertner, R. F., ''Photographic Study of Nucleate Pool Boiling on a Horizontal Surface,'' *ASME J. Heat Transfer*, **8**, 17 (1965).

Gorenflow, D., V. Knabe, and V. Bieling, ''Bubble Density on Surfaces with Nucleate Boiling—Its Influence on Heat Transfer and Burnout Heat Flux at Elevated Saturation Processes,'' *Proc. Int. Heat Transfer Conf.*, San Francisco, CA, Vol. 4, p. 1995 (1986).

Hosler, E. R., and J. W. Westwater, ''Film Boiling on a Horizontal Plate,'' *ARS J.*, **23**, 553 (1962).

Hsu, Y. Y., ''On the Size Range of Active Nucleation Sites on a Heating Surface,'' *J. Heat Transfer*, **86**, 207 (1962).

Judd, R. L., and A. Chopra, ''Interaction of the Nucleation Process Occurring at Adjacent Nucleation Sites,'' *J. Heat Transfer*, **115**, 955 (1993).

Judd, R. L., and K. S. Hwang, ''A Comprehensive Model for Nucleate Boiling Heat Transfer Including Microlayer Evaporation,'' *J. Heat Transfer*, **98**, 623 (1976).

Juric, D., and G. Tryggvason, ''A Front Tracking Method for Liquid-Vapor Phase Change,'' *ASME, FED*, **294**, 141 (1995).

Juric, D., and G. Tryggvason, ''Numerical Simulations of Phase Change in Microgravity,'' *ASME, HTD*, **332**, 33 (1996).

Kenning, D. B. R., ''Wall Temperatures in Nucleate Boiling,'' *Proc. Eurotherm. Semin, Adv. Pool Boiling Heat Transfer*, Paderborn, Germany, p. 1 (1989).

Klimenko, V. V., ''Film Boiling on a Horizontal Plate—New Correlation,'' *Int. J. Heat Mass Transfer*, **24**, 69 (1981).

Lay, J. H., and V. K. Dhir, ''A Nearly Theoretical Model for Fully Developed Nucleate Boiling of Saturated Liquids,'' *Proc. Int. Heat Transfer Conf.*, Brighton, England, Vol. 5, p. 105 (1994).

Lay, J. H., and V. K. Dhir, ''Shape of a Vapor Stem During Nucleate Boiling of Saturated Liquids,'' *J. Heat Transfer*, **117**, 394 (1995).

Mikic, B. B., W. M. Rohsenow, and P. Griffith, ''On Bubble Growth Rates,'' *Int. J. Heat Mass Transfer*, **13**, 647 (1970).

Mikic, B. B., and W. M. Rohsenow, ''A New Correlation of Pool Boiling Data Including the Effect of Heating Surface Characteristics,'' *J. Heat Transfer*, **9**, 245 (1969).

Melenkov, I. G., ''Detachment Frequency as a Function of Size of Vapor Bubbles,'' (Transl.), *Inzh. Fiz. Zh.*, **20**, 99 (1971).

Plesset, M. S., and S. A. Zwick, ''Growth of Vapor Bubbles in Superheated Liquids,'' *J. Appl. Phys.*, **25**, 493 (1954).

Qiu, D. M., V. K. Dhir, M. M. Hasan, D. Chao, E. Neumann, G. Yee, and J. Witherow, ''Single Bubble Dynamics During Nucleate Boiling Under Microgravity Conditions,'' Engineering Foundation Conf. on Microgravity Fluid Physics and Heat Transfer, Honolulu, HI (1999).

Ramanujapu, N., and V. K. Dhir, ''Dynamics of Contact Angle during Growth and Detachment of a Vapor Bubble at a Single Nucleation Site,'' *Proc. ASME/JSME Joint Thermal Eng. Conf.*, March 15−19 (1999).

Reimann, M., and U. Grigull, ''Warmeubergang bei Freir Konvektion und Filmsieden im Kritischen Gebit von Wasser und Koglendioxid,'' *Warme-und Stef-fubertragung*, **8**, 229 (1975).

Rohsenow, W. M., ''A Method of Correlating Heat Transfer Data for Surface Boiling of Liquids,'' *Trans. ASME*, **74**, 969 (1952).

Sakurai, A., M. Shiotsu, and K. Hata, ''A General Correlation for Pool Film Boiling Heat Transfer from a Horizontal Cylinder to Subcooled Liquid: 1. A Theoretical Pool Film Boiling Heat Transfer Model Including Ration Contribution and its Analytical Solution,'' *J. Heat Transfer*, **112**, 430 (1990a).

Sakurai, A., M. Shiotsu, and K. Hata, ''A General Correlation for Pool Film Boiling Heat Transfer from a Horizontal Cylinder to Subcooled Liquid: 2. Experimental Data for Various Liquids and its Correlation,'' *J. Heat Transfer*, **112**, 441 (1990b).

Sakurai, A., and M. Shiotsu, ''Pool Film Boiling Heat Transfer and Minimum Film Boiling Temperature,'' *Proc. Engineering Foundation Conf. on Pool and External Flow Boiling*, V. K. Dhir and A. E. Bergles, eds. Santa Barbara, CA p. 277 (1992).

Sernas, V., J. H. Linehard, and V. K. Dhir, ''The Taylor Wave Con-

figuration During Film Boiling from a Flat Plate,'' *Int. J. Heat Mass Transfer*, **16**, 1820 (1973).
Snyder, N. R., and D. K. Edwards, ''Summary of Conference on Bubble Dynamics and Boiling Heat Tranfser,'' Memo 20-137, Jet Propulsion Lab, Pasadena, CA (1956).
Son, G., V. K. Dhir, and N. Ramanujapu, ''Dynamics and Heat Transfer Associated with a Single Bubble During Partial Nucleate Boiling on a Horizontal Surface,'' *J. Heat Transfer*, **121**, 623 (1999).
Son, G., and V. K. Dhir, ''Numerical Analysis of Film Boiling Near Critical Pressure with a Level Set Method,'' *J. Heat Transfer*, **120**, 183 (1998).
Son, G., and V. K. Dhir, ''Numerical Simulation of Saturated Film Boiling on a Horizontal Surface,'' *J. Heat Transfer*, **119**, 525 (1997).
Staniszewski, B. E., ''Nucleate Boiling Bubble Growth and Departure,'' Tech. Rep. No. 16, Division of Sponsored Research,'' M.I.T., Cambridge, MA (1959).
Stephan, K., and M. Abdelsalem, ''Heat Transfer Correlations for Natural Convection Boiling,'' *Int. J. Heat Mass Transfer*, **23**, 79 (1980).
Sussman, M., P. Smereka, and S. Osher, ''A Level Set Approach for Computing Solutions to Incompressible Two-Phase Flow,'' *J. Comput. Phys.*, **114**, 146 (1994).
Vijaykumar, R., and V. K. Dhir, ''An Experimental Study of Subcooled Film Boiling on a Vertical Surface—Thermal Aspects,'' *J. Heat Transfer*, **114**, 169 (1992a).
Vijaykumar, R., and V. K. Dhir, ''An Experimental Study of Subcooled Film Boiling on a Vertical Surface—Hydrodynamic Aspects,'' *J. Heat Transfer*, **114**, 161 (1992b).
Wang, C. H., and V. K. Dhir, ''On the Gas Entrapment and Nucleation Site Density During Pool Boiling of Saturated Water,'' *J. Heat Transfer*, **115**, 670 (1993a).
Wang, C. H., and V. K. Dhir, ''Effect of Surface Wettability on Active Nucleation Site Density During Pool Boiling of Saturated Water,'' *J. Heat Transfer*, **115**, 659 (1993b).
Wang, C. H., *Experimental and Analytical Study of the Effects of Wettability on Nucleation Site Density During Pool Boiling*, PhD Thesis, Univ. of California, Los Angeles, (1992).
Wayner, Jr., P. C., ''Evaporation and Stress in the Contract Line Region,'' *Proc. Engineering Foundation Conf. on Pool and External Flow Boiling*, V. K. Dhir and A. E. Bergles, eds., Santa Barbara, CA, p. 251 (1992).

Manuscript received Mar. 10, 2000, and revision received Sept. 11, 2000.